International Journal of Heat and Mass Transfer 150 (2020) 119291

Contents lists available at ScienceDirect

International Journal of Heat and Mass Transfer

journal homepage: www.elsevier.com/locate/hmt

3-D computational investigation and experimental validation of effect of shear-lift on two-phase flow and heat transfer characteristics of highly subcooled flow boiling in vertical upflow

Jeongmin Lee, Lucas E. O'Neill, Issam Mudawar*

Purdue University Boiling and Two-Phase Flow Laboratory (PU-BTPFL), School of Mechanical Engineering, Purdue University, 585 Purdue Mall, West Lafayette, IN 47907, USA

ARTICLE INFO

Article history:
Received 23 August 2019
Revised 11 December 2019
Accepted 29 December 2019
Available online 18 January 2020

Keywords:
Two-phase flow
Subcooled flow boiling
Shear-lift force
CFD

ABSTRACT

The present study is focused on development of a 3-D computational approach to predict highly subcooled nucleate flow boiling in vertical upflow. Investigation of existing computational methodology based on Volume of Fluid (VOF) approach revealed fundamental weaknesses in modeling multiphase flows, which stems mostly from inadequate representation of shear-lift force on bubbles. A user defined function is adopted which provides detailed information relating to this important effect, and computed results are validated through comparison with experimental results and analytic predictions of single bubble trajectory. The computational method is then used to model the entire flow field for subcooled flow boiling in a rectangular channel heated on two opposite walls, and predictions are validated against FC-72 experimental data for four different mass velocities. Overall, computationally predicted interfacial behavior, flow pattern, and heat transfer parameters (wall temperature and heat transfer coefficient) show good agreement with experimental data. The model is also shown highly effective at predicting local phenomena (velocity and temperature profiles) not easily determined through experiments.

1. Introduction

1.1. Application of two-phase flow boiling for thermal management

While developments in modern cutting-edge technologies have led to many performance benefits, these benefits were achieved at the expense of greatly increased amount of dissipative heat. This is especially the case with electronic and power devices, which are found in such applications as supercomputers, electronic data centers, medical equipment, advanced military radar, directed energy lasers, aircraft and spacecraft avionics, hybrid vehicle power electronics, and energy storage system (ESS) batteries [1,2]. High power densities and dissipative heat fluxes encountered in these applications mean single-phase liquid cooling methods are no longer effective, as they cannot fulfill cooling requirements across operating conditions.

As thermal management has become an enabling technology for many modern applications, diverse two-phase methods have been proposed, utilizing boiling and its reciprocal process of condensation. Of these two, the former deals with heat acquisition from devices with high-flux surfaces by phase change from liquid to vapor, and the latter involves heat rejection to the ambient by returning the vapor to liquid state. The appeal of phase change methods is derived mostly from the coolant's natural ability to utilize its both sensible and latent heat.

Compared to condensation, boiling often represents the greater challenge for design engineers. This is due to greater difficulty in controlling pressure drop and heat transfer coefficient to obtain stable operation, often related to presence of instabilities in the system [3–5]. Furthermore, over-intense boiling can lead to critical heat flux (CHF), where vapor occlusion of heated surfaces leads to rapid temperature rise capable of destroying whole systems.

CHF is inarguably the most important design factor and safety parameter for all high heat flux controlled boiling applications. Overheating beyond CHF greatly reduces cooling performance, causing the device being cooled to physically burn out or melt down. In applications avoiding this risk, however, boiling is a very effective approach to cooling modern devices due to its ability to greatly increase heat transfer coefficient, thereby decreasing surface temperature for a given heat flux, helping minimize system weight and volume, and requiring relatively small amounts of coolant compared to single-phase liquid cooling. Also, depending on boiling regime and operating conditions, devices can be maintained at a fairly uniform temperature near the coolant's saturation

* Corresponding author.
E-mail address: mudawar@ecn.purdue.edu (I. Mudawar).

https://doi.org/10.1016/j.ijheatmasstransfer.2019.119291
0017-9310/

Nomenclature

a	half of bubble diameter
C_L	shear-lift coefficient
c_p	specific heat at constant pressure
$\mathbf{\Delta}c$	mesh (cell) size
d	diameter for circular tubes
E	energy per unit mass
F	force
F_b	buoyancy force
F_{cp}	contact pressure force
F_{du}	unsteady drag force
F_h	hydrodynamic pressure force
F_{qs}	quasi-steady drag
F_s	surface tension force
F_{sl}	shear-lift force
G	mass velocity
G_s	dimensionless shear rate
g	gravitational acceleration
H	height of flow channel's cross-section
h	heat transfer coefficient
h_{fg}	latent heat of vaporization
k	thermal conductivity
k_{eff}	effective thermal conductivity
L	total length of computational domainin individual references (Table 3)
L_d	development length of flow channel in experiment
L_e	exit length of flow channel in experiment
$L_{entrance}$	entrance length of computational domain
L_{exit}	exit length of computational domain
L_h	heated length of flow channel
$\dot{m}$	mass transfer rate
P	pressure
q''	heat flux
Re	Reynolds number
r_i	mass transfer intensity factor
S_h	volumetric energy source
T	temperature
T_{in}	temperature at channel inlet
t	time
t_s	thickness of solid wall in computational domain
ΔT_{sub}	inlet subcooling
U_r	relative velocity
u	velocity
u_τ	friction velocity
V	volume
W	width of flow channel's cross-section
y	coordinate normal to wall
y^+	dimensionless distance perpendicular to the wall
z	axial direction coordinate

Greek symbols

α	volume fraction; void fraction
θ_a	advancing angle
θ_i	inclination angle
θ_r	receding angle
μ	dynamic viscosity
ν	kinetic viscosity
ρ	density
ϕ	fluid property

Subscripts

b	bubble
f	liquid phase
g	vapor phase
i	initial bubble condition; index for phase
sat	saturation
sub	subcooling

temperature. Because of these practical merits, boiling schemes have been target of extensive investigations at the Purdue University Boiling and Two-Phase Flow Laboratory (PU-BTPFL) and other organizations worldwide. Configurations considered include capillary-pumped [6], pool boiling [7–9], macro-channel flow boiling [10–12], mini/micro-channel flow boiling [13,14], spray [15–17], jet impingement [18,19], and hybrid cooling schemes [20].

The present study is focused entirely on channel flow boiling. Presently, predicting two-phase flow and heat transfer in channels relies mostly on empirical correlations (*e.g.,* [21–25]) and, to a lesser extent, theoretical models [26,27]. For thermal design engineers in industry, correlations are highly desirable because of their ease of use, however, they are valid only for the specific fluid(s) and operating ranges of databases upon which they are based.

1.2. Utilization of computational methods for prediction of two-phase flow and heat transfer

The present study focuses on two-phase boiling flow and heat transfer characteristics in vertical upflow. Key points are to predict boiling regime and heat transfer coefficient under given operating conditions. To overcome the limitations of empirical correlations, computational approaches have gained increased popularity for thermal system design. Computational approaches have evolved over the past few decades along with improvements in computing performance of computer hardware. Computational methods have shown credible success in predicting single-phase fluid flow and heat transfer in a variety of flow configurations and operating environments, verified by agreement with experimental data. Over time, significant improvements in numerical schemes for enhanced accuracy, stability and computation speed have been made for complicated single-phase flows.

Computational prediction of two-phase flow involving phase change is still challenging, but continuing research is closing the gap with single-phase flow. One key facet of predicting two-phase flow is to track the interface between liquid and gas phases as behavior of each phase and interaction along interface define flow regime that in turn affects heat transfer. In the case of boiling, the behavior of vapor bubbles (*i.e.,* bubble departure, deformation, coalescence, and breakup) can determine the stage in the boiling process, and each stage has distinct heat transfer characteristics. A recent review article by Kharangate and Mudawar [28] introduced several interface tracking methods that have shown success in numerical modeling of multi-phase flow. Lagrangian and Eulerian methods are two such schemes. The former provides accurate and smooth interfaces between phases, but it is complex and computationally expensive because of the need to remesh every iteration. This method is suitable for modeling a single bubble or film-wise condensation with a simple flow configuration. On the other hand, Eularian methods are relatively less complicated and expensive, but show difficulty in clearly capturing interface (although some interface reconstruction schemes compensate for this weakness). Even Eulerian methods, however, require high performance computing resources if full scale, realistic boiling problems (*e.g.,* full micro-channel heat sinks) are to be simulated.

Another key factor in proper computational prediction of two-phase flows is modeling the phase change mechanism. In general, phase change models are combined two-phase schemes that track or capture interface position and evaluate mass transfer across the

interface. Selection of appropriate mass transfer model is critical to accurate computational predictions and will be discussed in greater detail in following sections.

The ability of the selected computational approach to fully capture crucial interfacial dynamics and heat/mass transfer at interfaces largely determines its ability to predict bulk flow phenomenon including flow regime and heat transfer. These small-scale, local calculations of mass, momentum, and energy transfer across interfaces are also common causes of numerical divergence if not configured properly for given boundary conditions. Many studies have focused on computational/numerical prediction of nucleate boiling (ONB) [29–31], slug flow [32], and annular flow [33] using computational modeling, with differing degrees of success predicting important design parameters such as wall temperature, heat transfer coefficient, and void fraction along flow channel.

Despite the proliferation of recent works regarding computational phase change modeling, many difficulties remain in selecting and utilizing proper sub-models (selecting and implementing a proper mass transfer model is particularly difficult depending on operating conditions under investigation). The following sections will discuss pros and cons of different approaches and outline the methodology adopted in the present study.

1.3. Choice and limitations of volume of fluid (VOF) method, and need for 3-D modeling

Of the two popular numerical methods for multi-phase flow, Eulerian has been more commonly used to track liquid-vapor interface due to the practicality of implementation. The most popular of Eulerian methods is the volume-of-fluid (VOF) model, which solves a continuity equation for the volume fraction of each phase and a single momentum equation throughout computational domain. Theoretically, volume fraction is a continuous function in time and space and only applicable in the case where each phase is not immiscible. VOF model is comparatively simpler, less time-consuming, and more stable in tackling mass conservation than another common approach called the level-set (LS) model, though it is less accurate in capturing interface topology. VOF model can also be easily combined with phase change models computing mass transfer between phases incorporated in the continuity equation, while LS model suffers numerical divergence associated with instability in mass conservation when tackling multi-phase flow with phase change.

In spite of these merits, VOF model often provides poor prediction of flows with a discrete fluid in a continuous fluid (*e.g.*, bubbly flow or mist/droplet flow) due to the absence of momentum equations for each phase. As a single set of momentum equations is shared by phases, forces acting at/across interfaces cannot be precisely calculated due to less accurate estimation of relative velocities between phases. Inaccurate force prediction for interaction between different phases leads to errors in predicting bubble detachment or lift-off (particularly in high-velocity convective boiling where these effects are critical), causing severe errors regarding bubble motion along the flow direction. These errors become even worse in the case of a few dispersed bubbles surrounded by continuous fluid and large difference in velocities between phases. In a previous study by the current authors relating to 2-D flow boiling simulations [34], it was clearly shown that streamlines penetrate across interfaces and there is no stagnation point around bubbles, as seen in Fig. 1. Hence, forces acting on bubbles can be under-/over-predicted, which causes pre-CHF at high heat flux conditions as a result of wrong prediction of bubble lift-off. One of the missing forces relating to the bubble lift-off is a transverse force called shear-lift force which a particle experiences when moving in a shear flow [35]. The influence of shear-lift force on lateral migration in shear flow for rigid spherical particles was first demonstrated experimentally by Segre and Silberberg [36]. Because of this effect, these particles have a certain equilibrium position in a tube, irrespective of the injected position. Similarly, treatment of the shear-lift force governing a bubble's lateral migration may have a profound effect on improving results for continuum flow model computations used to predict large-scale dispersed liquid-gas flows.

In addition to insufficient treatment of interfacial forces by current computational approaches, there is the possibility of large discrepancies between 3-D and 2-D boiling simulations not addressed in most prior works. As 3-D approaches fully consider all bounding walls of a flow channel, predicted shear stress is more accurate, affecting bubble behavior near the walls. Further differences between 2-D and 3-D simulations are attributable to differences in bubble shape, with bubbles close to sphere/semi-sphere in 3-D as opposed to cylinder or truncated cylinder in 2-D. This means area in contact with liquid phase will be different, affecting the amount

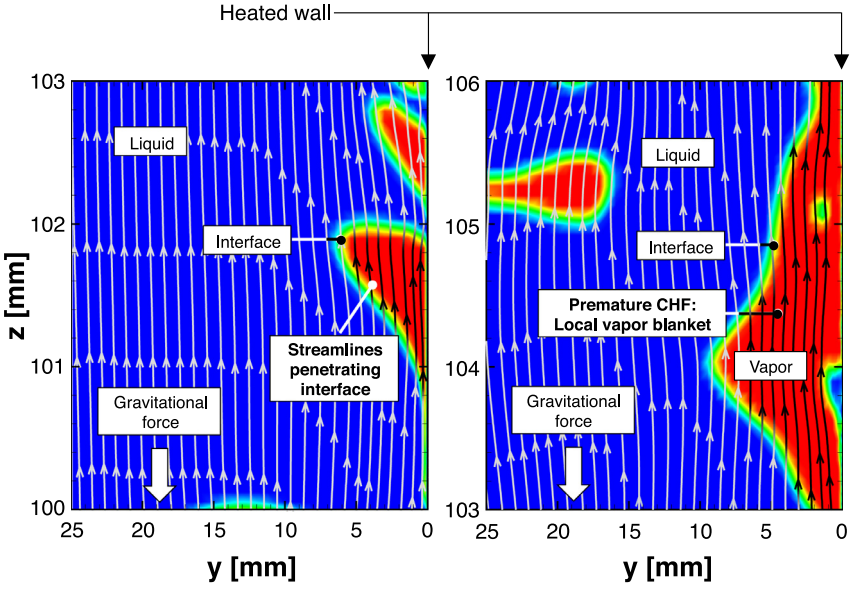

Fig. 1. Streamlines around vapor bubble in vertical upflow for G = 836.64–833.14 kg/m2s, q'' = 191–246 kW/m2 and $ATsub$ = 30.81–31.24 °C.

of phase change, which is a key factor of two-phase cooling. Moreover, unpredicted shear stress from sidewalls of a rectangular flow channel in 2-D tends to stimulate pre-CHF as shear-lift force from sidewalls (captured in 3-D simulations) pushes bubbles towards the channel center and aids liquid replenishment along the heated walls. In 2-D computations, absence of this extra shear effect leads to premature predictions of CHF. Thus, 3-D boiling simulation and accurate modeling of forces acting on bubble are crucial in the case of relatively large-scale computational domain with high heat flux conditions.

1.4. Objectives of study

The present study is a continuing part of NASA's Flow Boiling and Condensation Experiment (FBCE), an ongoing collaboration between NASA Glenn Research Center and the Purdue University Boiling and Two-Phase Flow Laboratory (PU-BTPFL). The primary goal of this initiative is to develop an experimental facility for the International Space Station (ISS) capable of gathering long term flow boiling and flow condensation data in microgravity that can be contrasted with data amassed from terrestrial experiments in order to develop predictive tools (empirical, analytical and computational) capable of accurately accounting for effects of body force on two-phase flow and heat transfer in channels. A summary of scientific developments realized as a part of the project can be found in a recent review article by Mudawar [37], including details of extensive prior flow boiling testing performed on ground and in parabolic flight [38,39].

The present study uses both experimental and computational results to explore fluid flow and heat transfer characteristics for highly subcooled vertical upflow of FC-72. The present computational approach offers significant improvements over prior work [34] by incorporating (1) modeling of shear-lift force acting on bubbles in forced convective boiling, and (2) simulating the full 3-D computational domain (including both fluid and solid sections for conjugate heat transfer). Conditions for four different mass velocities and heat fluxes are examined. Shear-lift force acting on vapor phase as well as the method of identifying effective bubble size influenced by this force are provided using a user-defined function (UDF). Validation of the effect of shear-lift force on bubble behavior in computational modeling is performed by comparing predictions for single bubble trajectory in a flow channel with experiments by Nahra and Motil [40]. Two other shear-lift models developed by Mei and Klausner [41] and Legendre-Magnaudet [35] are also numerically investigated. Vapor void fraction is used to validate set-up of phase change model relating to the mass transfer intensity factor incorporated in computational analysis as dominant interfacial diffusion that can arise from advection in 3-D. Temporal and spatial averaging method is employed to predict the wall temperature and heat transfer coefficient. Overall, this study investigates computationally important characteristics of flow boiling which cannot be obtained from experiment, including void fraction, velocity and temperature distributions for both along and across flow channel.

Key goals for the present work are:

1) Investigate benefits of scaling-up from a 2-D to a 3-D computational domain, evaluated in terms of accurate prediction of flow boiling hydrodynamics and corresponding heat transfer.
2) Further outline proper use of Lee mass transfer model [42] for subcooled flow boiling simulations, focusing on the use/non-use of identical values of mass transfer intensity factor (r_i) for interfacial evaporation and condensation calculations.
3) Illustration of the inability of current VOF formulation to capture interfacial behavior. A new approach to better account for interfacial forces (primarily the shear-lift force) will be outlined, and its benefits over the unmodified approach detailed.
4) Comparison of 3-D predictions (accurately accounting for interfacial forces) and prior 2-D results with experimental results to establish the new 3-D approach as state-of-the-art for prediction of flow boiling in macro-channels.

2. Experimental methods

Experimental flow boiling results are used throughout the present study to offer validation of computational predictions. Thus, it is relevant to provide a brief summary of experimental methods employed in gathering results.

The test section used in the current work is the Flow Boiling Module (FBM), part of NASA's Flow Boiling and Condensation Experiment (FBCE). Fig. 2(a) provides an exploded view of its construction, highlighting how it is comprised of three polycarbonate plates compressed between two aluminum support plates. The flow channel is milled out of the central polycarbonate piece, which is polished to optical-grade clarity, allowing detailed high-speed flow visualization measurements to be made.

Fig. 2(b) provides a schematic of the flow channel. The channel is rectangular with 2.5-mm width and 5-mm height, providing a 3.33-mm hydraulic diameter (meaning the test section is best described as a macro-channel). A 32.79-cm developing length is located just downstream of a flow straightener near the channel inlet, provided to ensure hydrodynamically fully developed flow at the inlet of the heated length. The 11.46-cm heated length is comprised of two copper slabs recessed into the right and left walls of the channel, each with six resistive heaters soldered to the back. Direct fluid temperature measurements are made using type-E thermocouples just prior to the flow straightener (module inlet) and at the end of the 6.09-cm exit length downstream of the boiling region (module exit).

Fig. 2(c) showcases the construction and instrumentation of the heated length, with type-E thermocouples mounted in the copper slab just upstream and downstream of consecutive resistors (the positions of these thermocouples are important as their measurements will be compared directly to computational predictions of wall temperature in later sections). As mentioned previously, optically polished polycarbonate sidewalls are left unobstructed to allow for simultaneous heat transfer and flow visualization measurements.

Finally, Fig. 2(d) provides a schematic of the flow loop used for experiments. Working fluid FC-72 (a dielectric manufactured by 3 M Company) is circulated using an Ismatech MCP-z magnetically coupled gear pump and first passes through a filter to remove any particulates. A turbine flow meter is used to measure flowrate, after which the fluid enters a Cast-X circulation heater (pre-heater) used to set inlet conditions at the test section.

The test section is mounted on a rotating platform to allow for testing in different orientations, although all results presented in the current work correspond to vertical upflow orientation. A variac is used to control power supplied to the heated walls, and simultaneous flow visualization images are captured at 2000 frames per second (fps) with a pixel resolution of 2040 $\times$ 174 spanning the entire 11.46-cm heated length.

Exiting the test section, flow passes through an air-cooled Lytron heat exchanger, used to return the working fluid to single-phase liquid, prior to passing an accumulator (used to compensate for volume changes associated with vapor production) and returning to the pump.

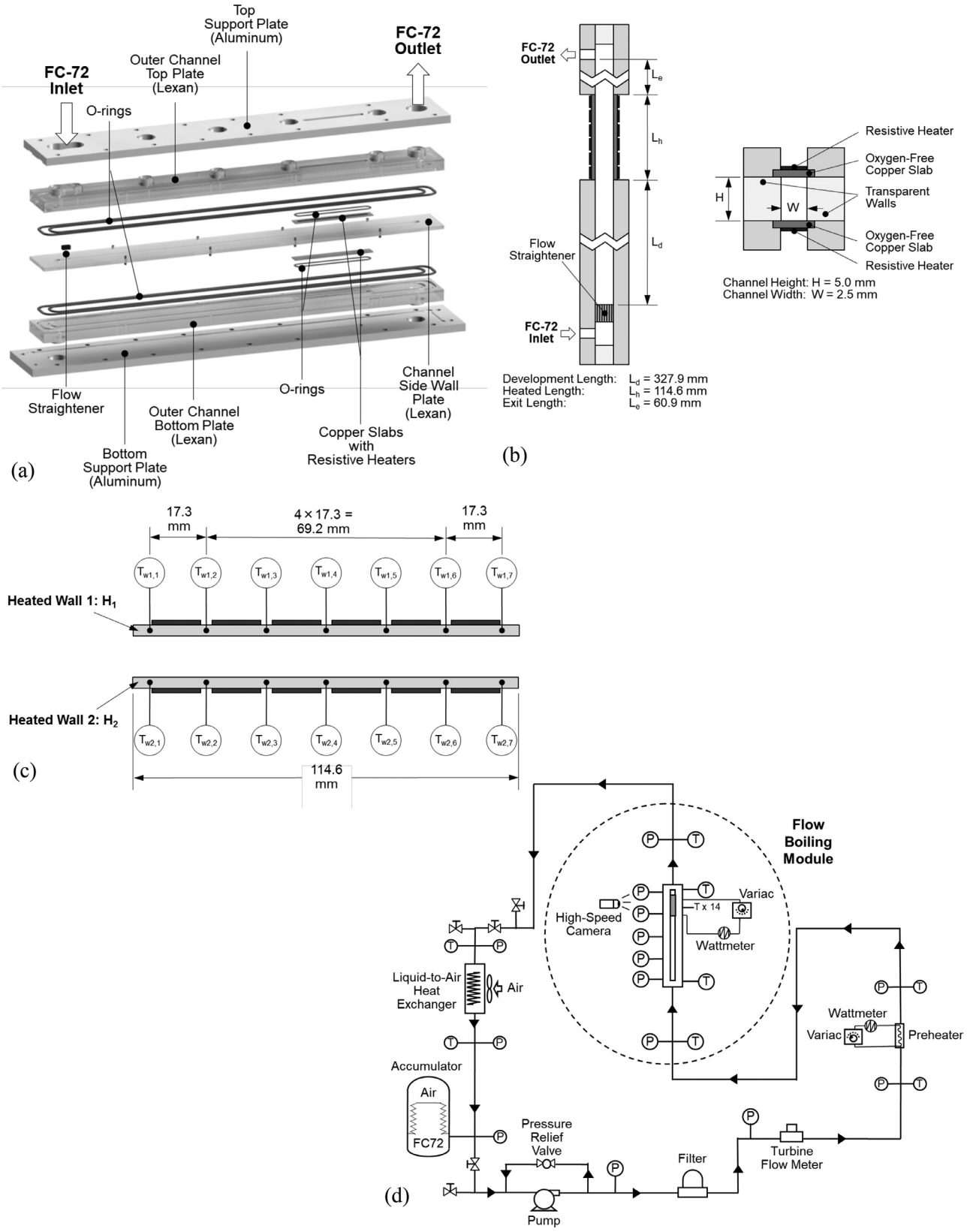

Fig. 2. (a) Exploded view of flow boiling module (FBM). Schematics of (b) FBM fluid path and (c) heated wall temperature measurement locations. (d) Schematic of flow loop.

All data collection is handled by a National Instruments NI SCXI-1000 data acquisition system controlled by LabView. Type-E thermocouples with an accuracy of ±0.5 °C are used to measure fluid and heated wall temperatures throughout the system. Pressure measurements are made using transducers with an accuracy of ±0.1% and pressure drop accuracy of ±0.2%. The turbine flow meter has an accuracy of ±0.1%, and wall heat input is measured with an accuracy of ±0.5 W. Overall uncertainty in determining the heat transfer coefficient is ±8%.

For additional details on fluid components used, measurement techniques employed, and operating conditions tested, the reader is advised to consult a prior experimental study [43].

3. Computational methods

3.1. Governing equations

A 3-D, transient, VOF approach is adopted in ANSYS FLUENT for tracking interfacial behavior during flow boiling with double-sided heated walls. Within this method, volume fractions of each phase are calculated for every computational cell and the sum of volume fractions of phases must equal unity. In order to obtain a sharp interface between liquid and vapor phases, spatial discretization scheme Geo-Reconstruct is explicitly used with interfacial anti-diffusion treatment (only applied to interfacial cells to suppress the excess numerical diffusion that can arise from 3-D advection effects and high aspect-ratio cells). Body force is implicitly considered to take into account vapor detachment from and liquid replenishment to the heated surface. It is assumed the flow is incompressible and properties of each phase are constant with temperature. Continuity of the volume fraction (including mass transfer between phases) is expressed as

$$\frac{\partial \alpha_f}{\partial t} + \nabla \cdot \left(\alpha_f \vec{u}_f\right) = \frac{1}{\rho_f} \sum \left(\dot{m}_{gf} - \dot{m}_{fg}\right) \text{ for liquid phase} \quad (1)$$

and

$$\frac{\partial \alpha_g}{\partial t} + \nabla \cdot \left(\alpha_g \vec{u}_g\right) = \frac{1}{\rho_g} \sum \left(\dot{m}_{fg} - \dot{m}_{gf}\right) \text{ for vapor phase,} \quad (2)$$

where α, $\vec{u}$, $\dot{m}$, and ρ are, respectively, volume fraction, velocity vector, mass transfer rate, and density. Subscripts f and g refer to liquid and vapor, respectively.

Momentum and energy equations are solved throughout the computational domain, with properties density, ρ, dynamic viscosity, μ, and thermal conductivity, k_{eff}, depending on local volume fraction. Momentum and energy equations are given by

$$\frac{\partial}{\partial t}(\rho \vec{u}) + \nabla \cdot (\rho \vec{u}\vec{u}) = -\nabla P + \nabla \cdot \left[\mu\left(\nabla \vec{u} + \nabla \vec{u}^T\right)\right] + \vec{F}, \quad (3)$$

and

$$\frac{\partial}{\partial t}(\rho E) + \nabla \cdot (\vec{u}(\rho E + P)) = \nabla \cdot \left(k_{eff} \nabla T\right) + S_h, \quad (4)$$

where P and E refer to pressure and energy per mass. All properties used in above equations are determined according to

$$\phi = \sum \alpha_i \phi_i, \quad (5)$$

where ϕ is the fluid property evaluated using a phase-weighted average of liquid and vapor values. The Continuum Surface Force model (CSF) [44] is used for surface tension force as a part of the source term $\vec{F}$ in the momentum equation. Similarly, the extra energy transfer from boiling and condensation is incorporated as a source term, S_h, in the energy equation. It is defined as the product of mass transfer rate and latent heat, expressed as $\dot{m}h_{fg}$. A shear-lift force acting on only the vapor phase is also included in the present formulation, which is discussed in next section. In addition, to consider turbulence effects in flow boiling, the two-equation Shear-Stress Transport (SST) k-ω turbulence model with turbulence dampening is used. This model is a combination of k-ω and k-ε models, applying the former in the near-wall region and the latter for free-stream flow (with a blending function applied between them). It has been observed the SST k-ω turbulence model shows improved prediction of temperature gradients near liquid-vapor interfaces, likely due to its treatment of turbulence dampening in this region. Use of the k-ω model in the near-wall region allows consideration of low Reynolds effects and shear flow spreading, capturing most physical phenomena of present in two-phase flows [44,45]. The use of another two-equation turbulence model, such as the k-ε model, was avoided as this offers less accuracy in the near-wall region. High-order turbulence models, while potentially more accurate, were also avoided as they incur high computational expense. Overall numerical details and discretization methods used in the present study are similar to ones applied in recent computational modeling of 2-D flow boiling by the present authors [34], with key differences being the 3-D domain and inclusion of shear-lift force in conservation of momentum in the present work.

3.2. Shear-lift force

Klausner et al. [46] and Zeng et al. [47] provided detailed analysis of forces acting on a bubble in directions parallel and normal to the heated surface to understand the influence of shear flow conditions on bubble detachment in flow boiling. Investigation of shear-lift force and wake effect acting on single and multiple bubbles (with sizes much larger than bubbles in the current study) in shear liquid flow was conducted computationally by Rabha and Buwa [48], showing good prediction of bubble trajectory, change in bubble shape, and vorticity distribution for rising dispersed bubbles. As bubble growth and detachment are important to the boiling process, force balance on bubbles should be carefully evaluated. As discussed in the introduction, however, forces generated by differences in phase velocities cannot be accurately evaluated because of limitations characteristic of the VOF method. As illustrated in Fig. 3, force balance for single bubble on vertical wall is given as

$$\sum \vec{F}_y = \vec{F}_{s,y} + \vec{F}_{du,y} + \vec{F}_{sl} + \vec{F}_h + \vec{F}_{cp} = \rho_g V_b \frac{d\vec{u}_y}{dt}$$
for forces normal to the surface, (6)

and

$$\sum \vec{F}_z = \vec{F}_{s,z} + \vec{F}_{du,z} + \vec{F}_{qs} + \vec{F}_b = \rho_g V_b \frac{d\vec{u}_z}{dt}$$
for forces parallel to the surface. (7)

In the above equations, F_s is surface tension force, F_{du} unsteady drag force (due to transient and asymmetrical bubble growth), F_{sl} shear-lift force produced by the velocity gradient, F_h hydrodynamic pressure force, F_{cp} contact pressure force (due to pressure difference between inside and outside of the bubble at the reference point), F_{qs} quasi-steady drag in the flow direction, F_b buoyancy force, and V_b volume of bubble. Also in Fig. 3, θ_a, θ_r, and θ_i are, respectively, advancing, receding, and inclination angle. In this formulation, dynamic effects of turbulence and interfacial waviness are ignored.

Among these forces, shear-lift force induced by shear rate of oncoming flow is carefully examined in the present study as it is poorly predicted by the VOF method and found to affect bubble lift-off significantly. In addition, for a typical bubble of around 0.3 mm, shear-lift force is of the same order of magnitude as surface tension and unsteady drag forces (occurring due to asymmetrical bubble growth which acts opposite to surface normal), and

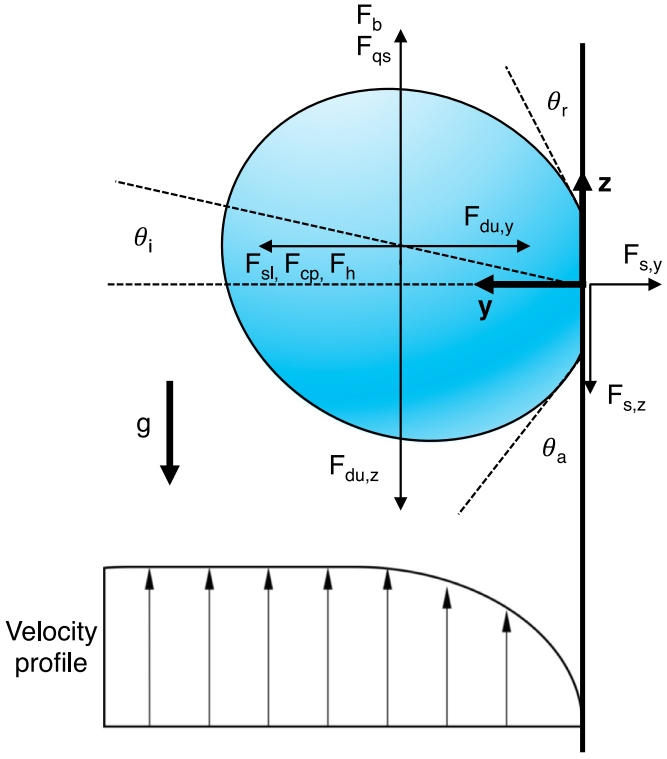

Fig. 3. Schematic of forces acting on single bubble on the heated surface in shear flow.

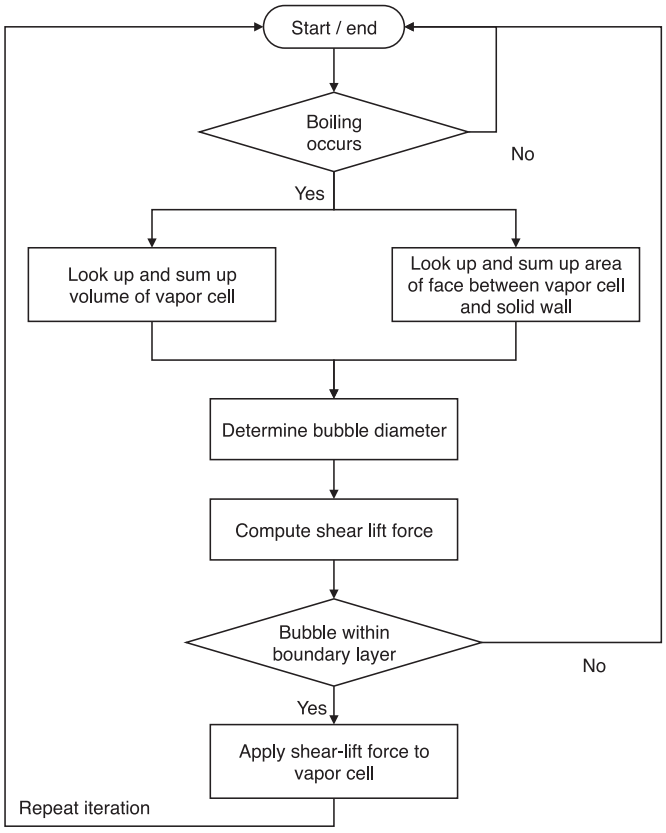

Fig. 4. Flow chart for computing and applying shear-lift force.

shear-lift has significant role in bubble detachment while the other forces play lesser roles [46]. For this study, models developed for a solid sphere in slow shear flow [49], a bubble in inviscid flow with weak shear [50], or in viscous linear shear flow [35] were excluded from analysis. To improve prediction of bubble behavior and thus heat transfer, the shear-lift force formulation derived by Mei and Klausner [41], considering local shear strain rate, is employed as a source term in the momentum equation using a user-defined function (UDF) in ANSYS FLUENT. It should be noted that they modified Saffman's model [49] to tackle vapor bubbles and, combined with Auton's study [50], developed an interpolation for the shear-lift force over a wide range of Reynolds number. Shear-lift coefficient in their formulation is expressed as

$$C_L = \frac{F_{sl}}{\frac{1}{2}\rho_f U_r^2 \pi a^2} = 3.877 G_s^{1/2} \times \left[\mathrm{Re}_b^{-m/2} + \left(0.344 G_s^{1/2}\right)^m \right]^{1/m}, \quad \text{with} \quad m = 4, \tag{8}$$

where

$$G_s = \left| \frac{dU_r}{dy} \right| \frac{a}{U_r}, \tag{9}$$

G_s is the dimensionless shear rate based on relative velocity, $U_r = U_f - U_g$, between the vapor bubble and liquid, Re_b is bubble Reynolds number based on the characteristic length of bubble diameter, and a is half the bubble diameter.

In order to apply these formulations to CFD, determining bubble diameter is most crucial for the current flow boiling application. It is both computationally complex and expensive to determine the diameter of every bubble along the flow channel as bubble size varies with time and space. In nucleate flow boiling, tiny bubbles are generated, and they get bigger downstream because of individual bubble growth and coalescence between bubbles. Further, as each bubble deforms in anisotropic fashion during flow boiling, it is hard to identify exact bubble diameter for every single bubble. Because of this complicating factor, the present study uses an average vapor bubble diameter (which changes in time) throughout the computational domain, updated every iteration according to the ratio of total vapor volume within the domain to interfacial area.

Another challenge is to identify the relative velocity between oncoming flow and bubble motion from the computational simulation. As fluid flow develops and nucleate boiling occurs, velocity vectors of oncoming liquid flow and the vapor motion within the bubble are not in the same direction, and they continue to change every iteration. Intense computational resources are required to perform the necessary integration and vector calculation for every single cell, so similar to that done in determining bubble diameter, the difference between constant liquid velocity and vapor velocity varying with space and time is used for relative velocity.

The detailed computing procedure for the UDF is described in the flow chart illustrated in Fig. 4. As subcooled liquid initially passes through the flow channel, shear lift force plays no role at the beginning. Once phase change occurs, this algorithm identifies cells occupied by vapor phase whose volume fraction is greater than or equal to a specific reference value of 0.5 and obtains total vapor volume within the entire domain through summation of cells with vapor. It also sums all face areas where vapor contacts the thermally conjugated surface between fluid and solid cells. These two values are saved into allocated memory, recalled by the UDF, and used to calculate the mean diameter of vapor every numerical iteration by dividing the total volume of vapor cells by the total surface area of vapor. Shear-lift force is then obtained according to Eq. (8). It should be noted that shear-lift force is only applied to the vapor cells within the velocity boundary layer (based on the velocity profile) because of the large shear rate in the boundary layer. This is necessary to prevent overestimation of shear-lift force, as overestimated positive and negative shear-lift forces would tend to squeeze the bubble and change

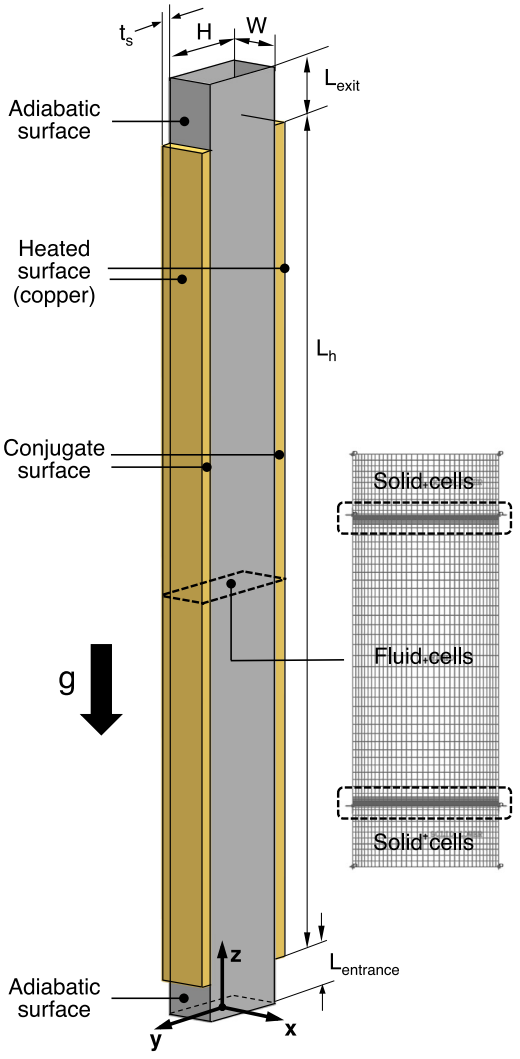

Fig. 5. Schematics of 3-D computational domain and mesh of cross section area.

its shape computationally to thin and long strings, which is not physically correct. The shear-lift force UDF is not applied if vapor cells are located beyond the velocity boundary layer (close to the core region). Validation of this methodology will be discussed in Section 4, performed through comparison with single-bubble experiments by Nahra and Motil [40].

3.3. Computational domain and initial/boundary conditions

Fig. 5 shows the computation domain used in the present study. This domain is three-dimensional and full sized, simulating vertical upflow boiling in a rectangular channel with cross sectional area of 2.5 mm × 5 mm ($W \times H$) and uses actual dimensions of copper heating walls used in the experimental flow boiling module. The length of domain is extended slightly to provide an adiabatic entrance length upstream ($L_{entrance}$ = 5 mm) and exit length downstream (L_{exit} = 10 mm), done to eliminate any potential numerically induced entrance/exit effects. Two solid regions of 2.5 mm × 1.04 mm × 114.6 mm ($W \times t_s \times L_h$), representing copper heating walls, are applied on the right and left of the fluid region to simulate conjugate heat transfer from solid to fluid. Meshing is done by ANSYS ICEM CFD, with quadrilateral mesh adopted for the entire domain. Non-uniform mesh sizing is used with refinement near walls to capture phase change starting from vapor embryos, bubble formation, and accurately predict shear stress and fluid-heat transfer interaction in the viscous sublayer.

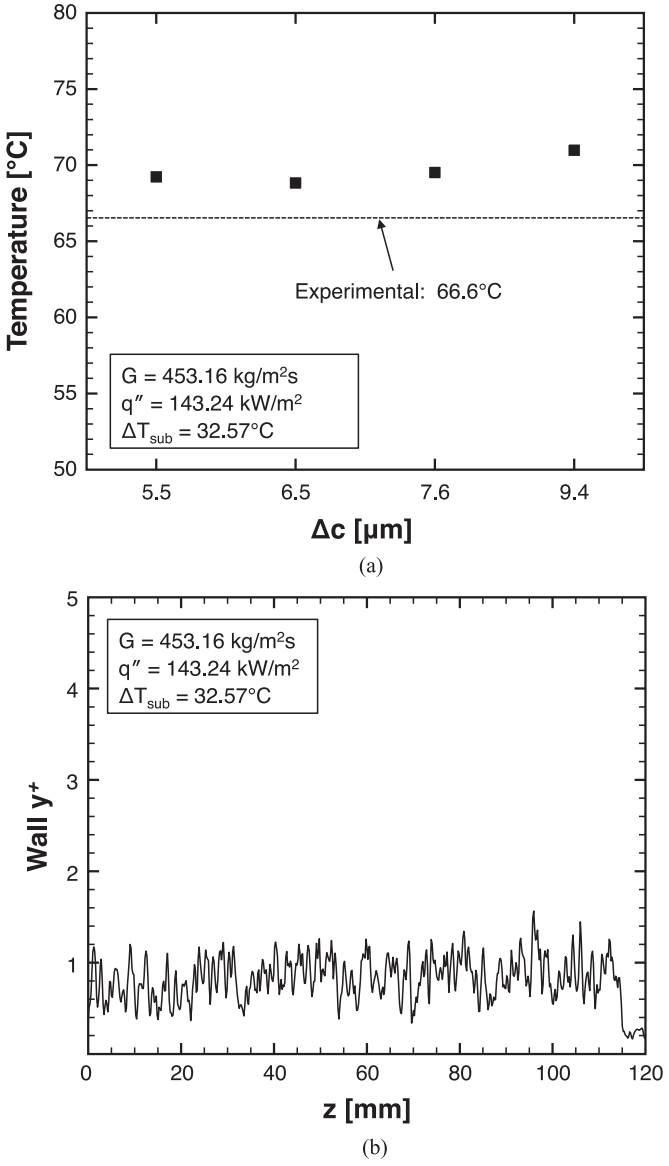

Fig. 6. (a) Grid independence test based on spatially and time-averaged wall temperature, (b) Axial variation of heated wall $y+$.

Grid independence is verified by averaging wall temperature over the entire copper heating walls for four different grid sizes, comparing the spatial and time averaged value with experimental data after reaching computational steady-state. For grid independence testing, intermediate mass velocity of G = 453.16 kg/m^{2}s and heat flux of q'' = 143.24 kW/m^2 are applied as boundary conditions. As shown in the authors' prior study involving 2-D simulation [34], near-wall cell size below 14-μm exhibited grid-independent results, so cell sizes of Δc = 5.5, 6.5, 7.5, 9.5 μm near wall are tested for the present 3-D simulation. Fig. 6(a) shows asymptotic convergence of average wall temperature achieved for near-wall cell size below around 7.5 μm. A cell size of Δc = 6.5 μm near wall is selected in the present study to provide peak accuracy with minimum computing time. As the present case corresponds to turbulent flow, it is also important to evaluate non-dimensional distance, y^+, from the wall based on the selected cell size. It is defined as

$$y^+ = \frac{y u_\tau}{\nu}, \tag{10}$$

Table 1
Mass velocities and thermophysical properties used in computational model.

G (kg/m^2.s)	T_{sat} (°C)	h_{fg} (J/kg mol)	ρ_f (kg/m^3)	C_{pf} (J/kg × K)	k_f (W/m · K)	μ_f (kg/m · s)	ρ_g (kg/m^3)	C_{pg} (J/kg · K)	k_g (W/m · K)	μ_g (kg/m · s)	σ (N/m)
176.52	61.97	2.775×10^7	1608.8	1117.1	0.0536	3.858×10^{-4}	15.874	942.06	0.0142	1.209×10^{-5}	0.0080
445.75	60.16	2.761×10^7	1605.2	1120.1	0.0534	3.786×10^{-4}	16.591	946.91	0.0143	1.215×10^{-5}	0.0079
836.64	62.20	2.974×10^7	1608.2	1117.6	0.0536	3.846×10^{-4}	15.992	942.87	0.0142	1.210×10^{-5}	0.0080
2453.51	69.37	2.701×10^7	1589.6	1133.1	0.0527	3.497×10^{-4}	19.953	967.97	0.0149	1.243×10^{-5}	0.0073

Table 2
Numerical details and discretization methods.

Pressure-velocity coupling	Pressure-implicit with splitting of operators (PISO)
Gradient	Least square cell based
Pressure	PRESTO!
Momentum	Third-order monotonic upstream-centered scheme for conservation laws (MUSCL)
Volume fraction	Geo-reconstruct
Turbulent kinetic energy	First-order upwind
Specific dissipation rate	First-order upwind
Energy	Second-order upwind
Transient formulation	First-order implicit

where y, u_τ, and v are, respectively, the absolute distance from the wall, friction velocity, and kinetic viscosity of mixture. Non-dimensional distance represents a standard measure of mesh refinement for heat and mass transfer phenomena of interest. This parameter fluctuates along the channel due to property variation and local phase change. As shown in Fig. 6(b), the selected cell size yields $y+ < 5$ along the heated wall for the entire channel length, which is small enough to capture relevant physical phenomena in the viscous sublayer.

Simulations for four different combinations of mass velocity and wall heat flux are performed in the present study. Fully developed velocity profiles corresponding to each mass velocity (G = 176. 96, 453.16, 837.32, 2438.28 kg/m^{2}s) and accompanying turbulent properties are applied at the inlet boundary. Specific pressure values equal to experimental data are used in the outlet boundary. No-slip boundary condition is applied to all walls. Contact angle estimated from the vapor-solid to vapor-liquid interface for wall adhesion effect is 175°. Contact angle influences wall adhesion effects in conjunction with the surface tension model [44], adjusting the curvature of the surface normal in cells near the heated surface and affecting the body force term during the surface tension calculation. Wall heat fluxes correspond to ~ 42–45% of CHF as measured during experiments [11] (corresponding to q'' = 104.34, 143.24, 191.56, 194.87 W/m^2). The range of inlet subcooling is between 30 and 36 °C. A coupled heat flux condition is applied to the interface between solid and liquid to address conjugate heat transfer. Indicated in Table 1 are properties of FC-72 for each case, which are determined based on the corresponding measured saturation pressure, spanning P = 113.82–151.83 kPa. Liquid initially occupies the entire flow channel with constant velocity corresponding to each mass velocity case. For numerical stability, a global Courant number ($u\Delta t/\Delta c$) of unity and variable time-step size ranging from 10^{-5} to 10^{-7} s are used. Full numerical details and discretization methods are summarized in Table 2.

3.4. Phase change model and mass transfer intensity factor in subcooled flow boiling

It is paramount to use an appropriate phase change model to achieve accurate computational prediction of heat and mass transfer. As the present study deals with highly subcooled liquid flow and begins from liquid-only state, mass transfer models that require pre-existing interfaces to calculate mass transfer (*e.g.*, Schrage model [51]) cannot be used. The Lee model [42] is adopted in the current approach due to its effectiveness at predicting evaporation in bulk flow at any location where fluid temperature exceeds local saturation temperature, and effectiveness of this model was verified in the authors' previous study [34]. The mass transfer rate per unit volume computed according to the Lee model is given by

$$\dot{m}_{fg} = r_i \alpha_f \rho_f \frac{\left(T_f - T_{sat}\right)}{T_{sat}} \text{ for } \quad \text{evaporation}, \tag{11}$$

and

$$\dot{m}_{gf} = r_i \alpha_g \rho_g \frac{\left(T_{sat} - T_g\right)}{T_{sat}} \text{ for } \quad \text{condensation}, \tag{12}$$

where r_i is mass transfer intensity factor, different values of which can affect evaporation and condensation rates. In regards to boiling, it is noted that r_i values can have an impact on growth of vapor bubble, interfacial behavior, flow regime, and total amount of heat rejection predicted along the flow channel. Generally, high r_i values can cause unstable numerical convergence while low r_i values can result in a discrepancy between interface and saturation temperatures.

Table 3 provides a summary of literature relating to computational flow boiling and flow condensation work performed using the VOF method with the Lee mass transfer model. Combination of VOF method and Lee model is the most easily implemented approach among those available for computational two-phase flow modeling and is capable of predicting a wide range of flow regimes including bubbly, slug, and stratified/wavy flow, rendering it a popular choice for design predictions of two-phase cooling applications. However, lack of understanding on how best to determine r_i value can limit its correct application in industry. Of special importance to the current study is appropriate determination of r_i in 3-D simulations that accounts for prevailing operating conditions, fluid properties, and flow geometry. Notice that all studies listed in Table 3 employ identical r_i values for both evaporation and condensation in Eqs. (11) and (12), respectively.

Firstly, use of identical r_i values for evaporation and condensation is dependent on how much fluid is subcooled or superheated. Most studies in Table 3 deal with low subcooling or saturated flow conditions. In this case, numerical error arising from r_i value (which can yield discrepancies between interfacial and saturation temperatures) is relatively minor. However, as high subcooling of around 34 °C is considered in present study, interfacial heat diffusion is significant, making interface-tracking difficult and accelerating vapor bubble condensation in non-physical fashion. Secondly, in regards to geometry (especially cross-section area), the

Table 3
Summary of computational works on channel flow condensation and flow boiling employing volume-of-fluid method and Lee mass transfer model.

Author(s)	System	Dimensions	Refrigerant	Operating conditions			Mass transfer intensity factor (r_i)
				ΔT_{sub} [°C]	G [kg/m^{2}s]	q'' [kW/m^2]	
Chen et al. [52]	Rectangular micro-channel (3D) Flow condensation	L = 300 mm H = 1 mm W = 1 mm	FC-72	0	100–150	10–30	100
Wu et al. [53]	Serpentine tube (3D) Flow boiling	L = 560 mm d = 6 mm	R141B	3	40–200	7–36	0.1
Yang et al. [54]	Coiled tube (3D) Flow boiling	L = 842.6 mm d = 6 mm	R141B	8–10	120–180	7–25	100
Bahreini et al. [55]	Vertical mini-channel (2D) Flow boiling	L = 200 mm H = 6 mm	HFE-7100	5	20–210	20–160	1
Lorenzini & Joshi [56]	Micro-channel (3D)	L = 5, 6 mm	Water	0–10	500	0 –2700 (Non-uniform)	0.1
	Flow boiling	H = 150, 100 μm W = 300, 200 μm					
De Schepper et al. [57]	Single circular channel Flow boiling	L = 11.3 m d = 52.5 mm	Gasoil	30	336.759	30.6–44.2	0.1
Fang et al. [58]	Micro-channel	L = 5 mm H = 150 μm	Water	3.5	269.73	60–250	100
	Flow boiling	W = 300 μm					
Alizadehdakhel et al. [59]	Thermosyphon	L_h = 40 mm	Water	–	–	14.7–29.3	0.1
	Pool boiling and condensation	d = 1.75 cm					

present setup is quite small. While entire micro-channels can be engulfed by the thermal boundary layers, in macro-channels (such as the present setup), there are core regions not covered by the thermal boundary layers. These regions interrupt bubble production, growth and existence along the flow channel by allowing for entrainment and collapse (depending on local subcooling) of bubbles produced along the heated walls. Lastly, thermal conductivity and velocity of working fluid are also important factors. During transient computations of subcooled flow boiling, for a given time step, heat is quickly transferred to the subcooled core region while fluid with low thermal conductivity (vapor phase) cannot transfer heat, influencing development of the thermal boundary layer. Furthermore, subcooled flow with high velocity can flush out the boundary layer or cause generation of a thin thermal boundary layer, which is not a favorable environment for computational predictions of phase change. Thus, use of identical r_i values for both evaporation and condensation in the Lee model is a good assumption only in cases with low subcooling or saturated inlet, small sized cross-section area, fluid with high thermal conductivity, and low inlet velocity. It must be noted that the value of r_i should be theoretically different for evaporation and condensation [60], but it is not trivial to tune these values to match experimental data because of unknown, undefined, or inconsistent variables such as bubble diameter, interface shape, and accommodation coefficient; these are important factors required to obtain evaporation-condensation flux developed from the Hertz-Knudsen formula and kinetic theory.

The operating conditions in this investigation (highly subcooled FC-72, low thermal conductivity, high flow velocity, macro-channel) mean use of identical r_i values is no longer effective. Fig. 7 compares, for G = 453.16 kg/m^{2}s, q'' = 143.24 kW/m^2, and T_{sub} = 32.57 °C, bubble formation predicted by the Lee model with (i) identical mass transfer intensity factor value, r_i = 100, used for both evaporation and condensation, and (ii) different values, r_i = 100 for evaporation and 0.1 for condensation. Predicted vapor bubble formations within the channel show appreciable discrepancy from experimental results in the case with identical r_i values for evaporation and condensation. It is obvious that void fraction predicted using identical r_i is much smaller due to much faster condensation of vapor bubbles by surrounding subcooled liquid, and consequently unrealistic depiction of bubble formation. On the other hand, use of different r_i values for evaporation and condensation predicts bubble formation and behavior (including growth, coalescence and departure) that are closer to those observed exper-

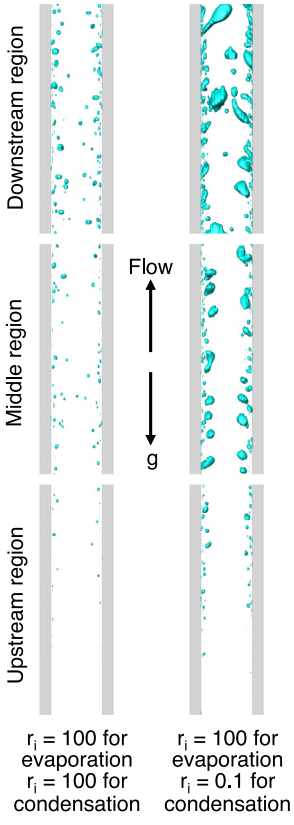

Fig. 7. Comparison of the influence of using identical versus different values for evaporation and condensation in the Lee model on vapor bubble formation along the channel.

imentally. Unfortunately, quantitative comparison cannot be conducted due to inherent difficulties present in calculating experimental void fraction using only 2-D images. In 2-D images, a large number of bubbles are piled up and randomly deformed, so it is difficult to track exact outlines of every single bubble and calculate volume of vapor present at any given moment. Comparison of average heated wall temperature was performed, but the temperature difference was small even though distinct differences in bubble formation were observed.

To finally determine most appropriate r_i value for evaporation in 3-D flow boiling, five different values (10, 100, 300, 500, and 1000) are examined and $r_i = 100$ (along with $r_i = 0.1$ for condensation) is selected based on thorough assessment of ability to predict experimental bubble formation, interfacial behavior, and wall temperature.

4. Results and discussion

4.1. Impact of shear-lift force

Shear-lift force plays a critical role in the bubble detachment process for cases where high flow inertia liquid occupies most of the flow channel and acts to suppresses formation and growth of small vapor bubbles produced on the heated surface. In order to validate the effectiveness of the present computational methodology at capturing shear-lift force, a sample case simulating a single bubble's lift-off and trajectory after detachment is examined and compared to experimental data as well as analytic models. To better capture the effect of the shear-lift force, a single vapor bubble under microgravity conditions is considered, thereby eliminating any influence of buoyancy force. Analytic trajectory calculations are performed using the models of Mei and Klausner [41] and Legendre and Magnaudet [35] for shear-lift and analyzing force balance of a bubble moving in Poiseuille flow as a function of time. For the force balance, drag force, shear lift force, and momentum terms including virtual mass force are considered. Computational predictions with and without the UDF for shear-lift force are performed for comparison. The 2-D computational domain for this simple case is illustrated in Fig. 8(a) along with actual dimensions of the experiment [40] used for validation. The adiabatic channel is 40-cm long and 2-cm high and contains air-water flow. Fully developed velocity profile is used for inlet boundary, and mean liquid velocity is 7 cm/s. A 4.5-mm diameter bubble with initial velocity components $u_i = 2.8$ cm/s (parallel to the wall) and $v_i = 2.0$ cm/s (perpendicular to the wall) is generated with its center 0.43 cm away from the wall.

Fig. 8(b) compares experimental single bubble trajectory with those calculated using analytic (solved numerically) and computational methods. It shows the computational method using the UDF for shear-lift force provides best agreement with experiment. It also illustrates how the bubble rapidly moves upwards because of strong shear-lift force near the wall. As the bubble migrates, relative velocity between the two phases gets smaller, reducing shear-lift force, and converges towards the channel centerline ($y = 1.0$ cm) due to equilibrium of positive and negative shear-lift forces at this point. Trajectory predicted computationally without inclusion of the UDF for shear-lift force also shows the bubble approaching the channel's centerline, albeit at a much

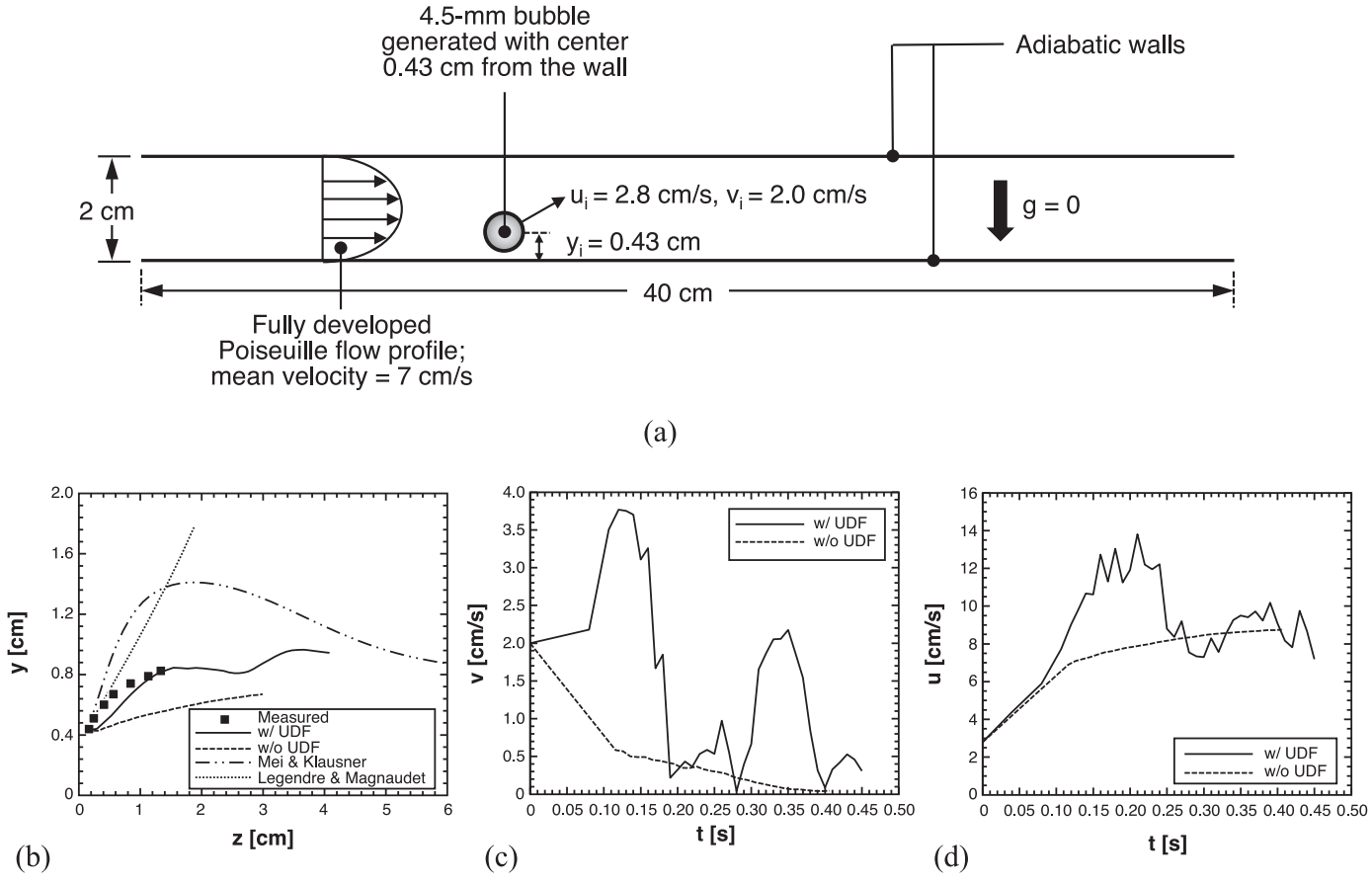

Fig. 8. (a) Example of single air bubble released in adiabatic Poiseuille water flow, which is used for evaluating effectiveness of present computational methodology at capturing force balance on a bubble, (b) Comparison of single bubble trajectory using experimental, computational, and analytic results, and investigation into the effect of user-define function (UDF) on the bubble's (c) normal velocity and (d) axial velocity.

slower rate than observed experimentally and predicted when using the UDF. This shows how, without the UDF, there is no additional force acting on the bubble in the transverse direction, and initial *y*-velocity is dominant in determining bubble motion. This is also proven in Fig. 8(c), which shows, without the UDF, *y*-velocity exhibits a monotonic decrease with time, while with the UDF initially increases above its initial velocity, then decreases because of negative force in the *y* direction, before fluctuating some as the bubble approaches the channel centerline. These differences in *y*-velocity also manifest in *x*-velocity, Fig. 8(d), as the case with the UDF shows the bubble penetrates the high-velocity liquid core earlier and is significantly accelerated, while that without the UDF, shows the bubble remains in the near-wall region for far longer.

It is important to point out that, with the UDF, Figs. 8(c) and 8(d) also capture the instantaneous fluctuations of *x*- and *y*-velocities, which are the outcome of ability to account for spatial and temporal variations of local liquid velocities surrounding the vapor bubble as the bubble rises and deforms, which also affect the bubble trajectory. On the other hand, without the UDF, changes in local velocities of liquid caused by bubble rise are not predicted, which results in non-physical smooth bubble drift along streamlines determined mainly by the inlet liquid profile.

Fig. 8(b) also shows how, when it comes to analytic calculations based on force balance for single bubble moving in time and space, the Mei and Klausner model over predicts bubble trajectory as virtual mass force (which is the inertia added to a bubble because an accelerating or decelerating bubble must push its way through surrounding liquid) cannot be carefully calculated every iteration. It still ends up converging into the core region of the flow channel, however, due to shear-lift working in the opposite direction after it initially overshoots the centerline. On the other hand, the Legendre and Magnaudet model predicts the bubble linearly lifts off away from the initial location. This model considers only relative velocity between a bubble and liquid flow velocity to calculate the shear-lift force, but not any other local fluid flow characteristics. Overall, both analytic solutions neglect to consider interfacial behavior, bubble deformation, or other local interactions between the bubble and surrounding liquid, meaning projected area for drag and shear-lift forces is assumed constant with time. This is a key area where the computational approach has a clear advantage, evidenced by the computational approach with modified shear-lift modeling providing best predictions of bubble lift-off and trajectory.

4.2. Fluid flow and heat transfer characteristics of highly subcooled boiling predicted by 3-D computational model with shear-lift force UDF

Fig. 9 shows computational visualization results obtained using the aforementioned computational method with the shear-lift UDF. Captured are images of flow boiling along the entire heated length as well as enlarged discrete regions (upstream, middle and

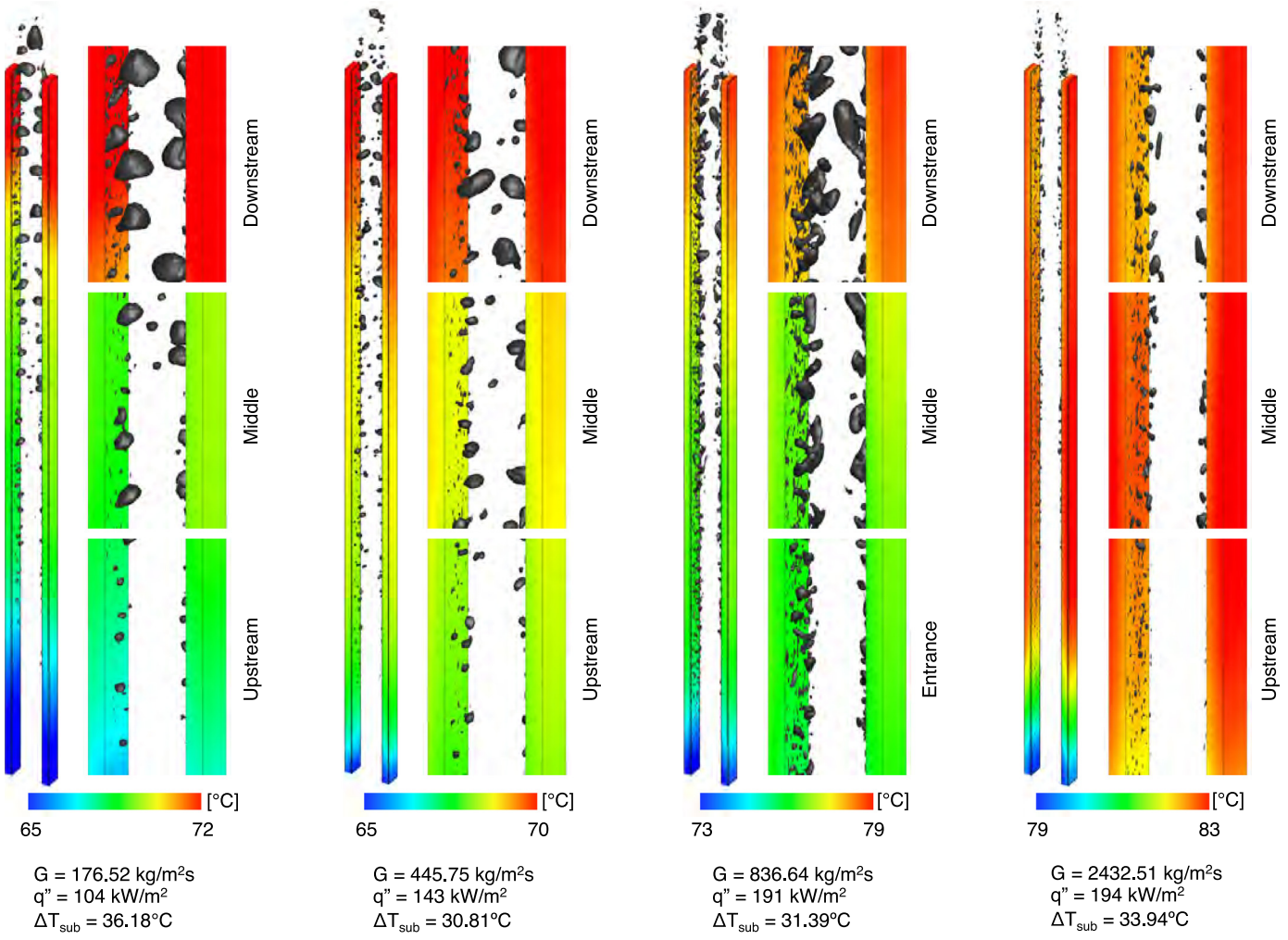

Fig. 9. Computationally predicted flow visualization images of entire heated channel for different mass velocities and different heat fluxes corresponding to fairly similar percentage of CHF.

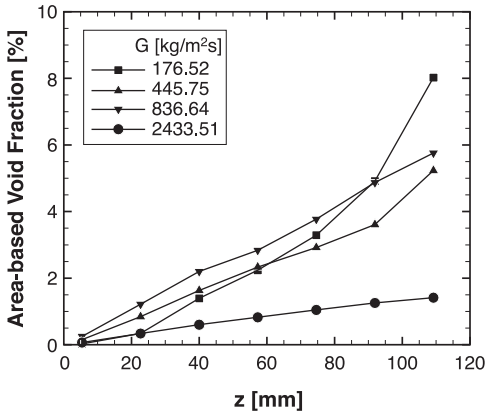

Fig. 10. Comparison of computed axial variations of vapor void fraction for four different mass velocities.

downstream) for vertical upflow boiling with highly subcooled inlet conditions and mass velocities of G = 176.52, 445.75, 836.64, and 2432.51 kg/m^{2}s. Heat fluxes in each case are different, but are all about 43% of CHF. Individual images illustrate instantaneous and temporal tracking of interfacial behavior and wall temperature contours corresponding to each set of operating conditions.

Vapor growth, bubble departure, entrainment, coalescence, and break-up are key facets of subcooled flow boiling. In Fig. 9, pure liquid with high subcooling of approximately 33 °C enters the heated portion of the flow channel, and tiny bubbles begin to form in entrance region. These bubbles grow in the axial direction as they coalescence and the rate of condensation diminishes due to increasing bulk fluid temperature along the channel. Vapor bubbles in the downstream region are seen to partially detach from the surface and migrate towards the liquid core. All heated wall phenomena observed are almost symmetrical in the computational results, but not exactly identical because of differences in small scale wake effects and rate of local vapor collision and bubble coalescence.

Fig. 9 shows obvious differences between cases with high mass velocities and those with lower mass velocities. As mass velocity increases, deformation of vapor bubbles is appreciable and pinching of vapor bubbles becomes noticeable, leading large bubbles to break into small discrete bubbles in the downstream region. This is largely due to strong shear stresses generated from both heated and adiabatic surfaces for higher mass velocities. Bubble shape is also seen to be less spherical than that under low mass velocity conditions.

For the highest mass velocity case of G = 2432.51 kg/m^{2}s, single-phase convection plays an important heat transfer role, small bubbles generated along the surface are unable to grow into large bubbles because of the ability of bulk liquid with high inertia to maintain its subcooling along the entire channel, and a thin thermal boundary layer is maintained along the entire channel. High flow velocity in this case also prevents any gradual evaporation due to minimal residence time along the heated walls. These effects make only a few computational cells near heated surfaces satisfy the saturation requirement for boiling (as outlined for the Lee mass transfer model), which results in decreased vapor void fraction. Fig. 9 also shows the variation of surface temperature between inlet and exit is around 5.5 °C for all mass velocity cases. This is evidence flow boiling is highly effective at maintaining relatively uniform temperature compared to purely single-phase heat transfer.

Axial variation of vapor void fraction along the channel is quantitatively examined to understand the influence of mass velocity on vapor generation. Fig. 10 compares vapor fraction for G = 176.52, 445.75, 836.64, and 2432.51 kg/m^{2}s computed at seven axial locations (z = 5.4, 22.7, 40.0, 57.3, 74.6, 91.9, and 109.2 mm) then spatially and time-averaged after reaching steady state. As distortion of bubble shapes becomes severe as mass velocity increases, improper guesses of bubble shape from experimental video images can cause serious errors when attempting to estimate local void fraction. This is why, unlike the authors' prior 2-D work [34], experimental results are not compared with the present 3-D computational void fraction results. Overall, predicted vapor void fraction in the present study shows a trend similar to that seen in the previous 2-D study. However, because the fraction of cross-sectional area occupied by liquid is much larger than by vapor in the 3-D simulations, void fraction values here are lower than those from the 2-D simulations.

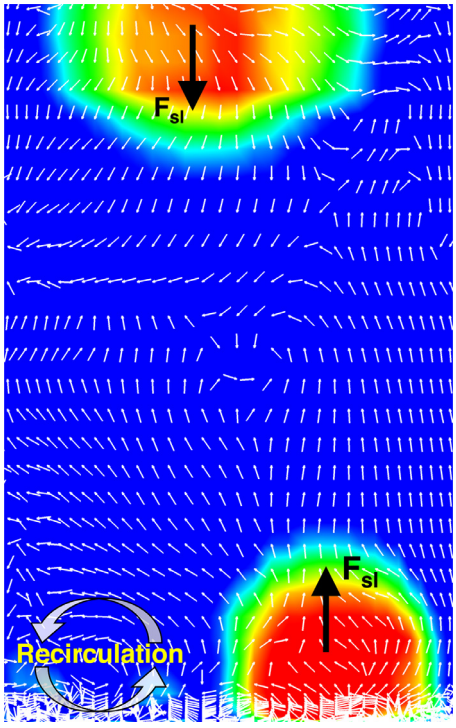

Fig. 11. Vector field of cross-sectional area volume-of-fraction contours at z = 79.2 mm for G = 176.52 kg/m^{2}s and q'' = 104 kW/m^2.

Fig. 10 shows void fraction starts from very low values (less than 1%) in the upstream region and increases gradually towards the exit for all cases. The results (excepting the highest mass velocity case) show large increments of void fraction with distance. The lowest velocity case in particular shows void fraction increases rapidly after the fifth point (z = 74.6 mm) where large bubbles are observed after coalescence begins to occur. It is interesting that values of void fraction for all cases except the highest mass velocity are somewhat similar despite predicted bubble sizes and interactions between bubbles differing, as shown in Fig. 9. Results for the highest mass velocity case, meanwhile, highlight how increased velocity suppresses bubble growth, stimulates bubble break-up, and invigorates condensation, resulting in very small void fractions in the range of ~ 0–2%.

Fig. 11 depicts instantaneously captured vector field in cross-sectional area at z = 79.2 mm along with a volume-of-fraction contour plot for G = 176.52 kg/m^{2}s and q'' = 104 kW/m^2. This figure captures the moment two large bubbles attached each to an opposite surface begin to depart. It is clear only one vector field for both liquid and vapor exists due to formulation of the VOF method as described previously. However, the UDF added shear-lift force F_{sl} acts on the cell occupied by vapor as an extra source

term in the momentum equation, yielding the detailed 3-D vector field with components vectors u (x-direction), v (y-direction normal to the surface), and w (z-direction), which are projected onto the x-y plane in Fig. 11. Inside vapor cells (red color) F_{sl} points in a direction normal to the surface.

This 3-D simulation also shows a large recirculation zone next to the lower bubble, which may contribute additional phase change by increasing liquid replenishment into near-wall region and encouraging further nucleation; an effect that cannot be captured in 2-D simulations. This is further validation that shear-lift both affects bubble detachment and enhances heat transfer by generating recirculation zones.

4.3. Validation of computed results

To more explicitly highlight advantages of moving from 2-D to 3-D simulations, Fig. 12(a) provides a comparison of flow visualization predicted by 2-D and 3-D computational methods (including the shear-lift modeling) with that captured experimentally. The lowest mass velocity case of $G = 176.52$ kg/m^{2}s with $q'' = 104$ kW/m^2 is excluded since it was not computed in the previous 2-D study. Predicted flow regimes from 3-D simulations are similar to both 2-D and experimental results. Even though more bubbles are generated in 3-D simulations compared to 2-D, this may be attributed to the increase in heated wall area in contact with liquid. Interfacial behavior from 3-D simulations is also in good agreement with experiments as well as 2-D simulations, and any over- or under-prediction of shear-lift force acting on vapor phase using the formulation described in Section 3 are not noticeable. But one interesting difference is the location where nucleate boiling initiates in 3-D simulation is further upstream compared to 2-D.

Fig. 12(b) shows a comparison of channel-averaged steady-state wall temperature versus mass velocity from 2-D and 3-D simulations alongside experimental results. This plot clearly shows the superiority of the present 3-D computational work with modified shear-lift modeling over the prior 2-D results as the 3-D curve is noticeably closer to experimental values for each mass velocity. Additionally, 3-D results match the slope of the experimental curve exactly, while 2-D results show a departure as mass velocity is increased. For the lower mass velocity case ($G = 445.75$ kg/m^{2}s), average wall temperature predicted by 3-D simulation is only ~2 °C greater than the experimental value, while the 2-D simulation predicts a value ~7 °C higher. These differences increase with increasing mass velocity, with 3-D results offset from experiments by ~5 °C for both $G = 836.64$ and 2432.51 kg/m^{2}s cases, while 2-D results over-predict temperature by ~15 °C and ~25 °C, respectively. The superiority of 3-D simulations results from the increased area for phase change, additional turbulent and wake effects in the span direction (produced by shear stress from the adiabatic sidewalls), and increased bubble departure rate due to the shear-lift force. Bubble detachment is suppressed by liquid with high inertia in 2-D simulations, but modified shear-lift modeling in the present 3-D work makes bubbles behave more physically.

Fig. 13(a) and 13(b) show wall temperature and heat transfer coefficient variations along the heated portion of the channel. Here, cases with four different mass velocities and heat fluxes are compared with one another. All values presented in this figure are spatially and time-averaged over a few seconds of steady-state simulation. Results from the authors' prior 2-D computational simulations [34] are averages of left and right wall values, while those from present 3-D simulations are indicated for each wall separately.

Fig. 13(a) shows wall temperature increases in the entrance region for all mass velocities tested due to dominance of single-phase heat transfer in this region (despite some minimal vapor generation as shown in Fig. 9). This entrance region corresponds

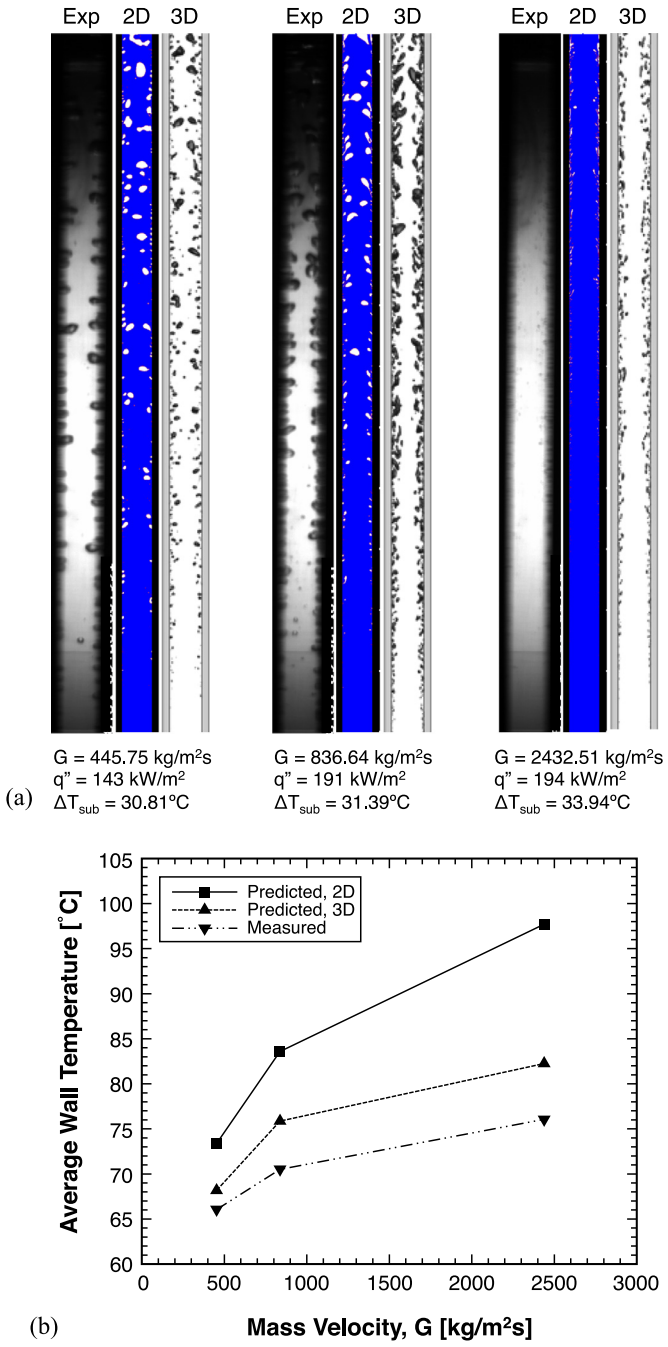

Fig. 12. (a) Comparison of flow visualization from experiment with predictions of present 3-D computational method and authors' previous 2-D method [34], (b) Comparison of corresponding average wall temperature with mass velocity.

to the surface from $z = 0$ mm to ~20 mm. Temperature difference between experimental results and 3-D simulations is minimal for the lowest mass velocity and increases slightly with increasing mass velocity. Once nucleate boiling begins, 3-D predicted wall temperature is largely constant along the channel, with values near 67 °C for the cases of $G = 176.52$ and 445.75 kg/m^{2}s, 75 °C for $G = 836.64$, and 81 °C for $G = 2432.51$ kg/m^{2}s. This is seen as a sizable improvement compared to 2-D simulation results, which show values that are both higher than measured and continuously increasing in the axial direction due to artificial vapor adhesion to the heated walls, which is rectified in the 3-D simulations through modified shear-lift modeling. The improvement with 3-D simulations is most noticeable for the highest mass velocity case, with

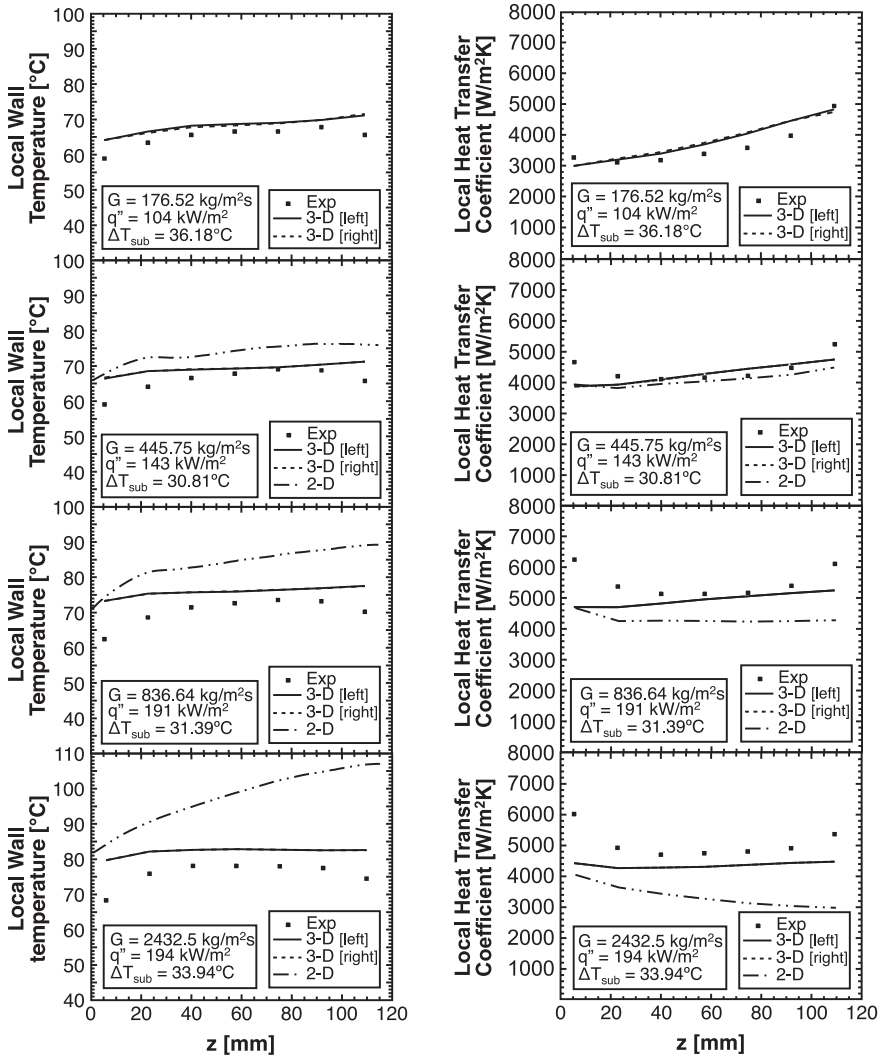

Fig. 13. Comparison of measured axial variations of (a) wall temperature and (b) heat transfer coefficient with predictions using present 3-D computational method and authors' previous 2-D method [34].

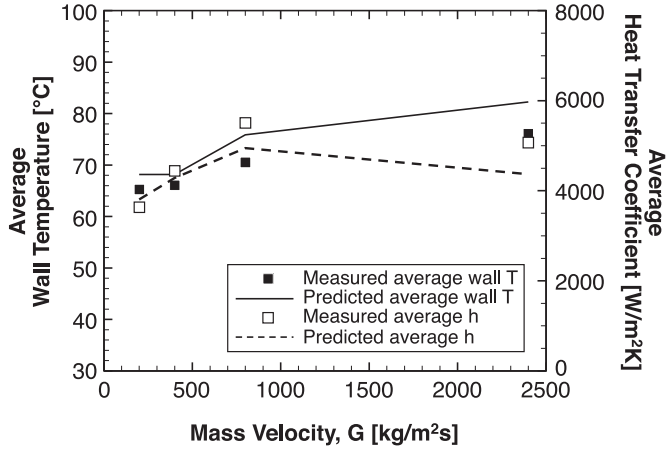

Fig. 14. Comparison of measured and 3-D computed average, wall temperature and average heat transfer coefficient for four different mass velocities.

predicted wall temperature in the present study 20–25 °C lower than 2-D results in the middle and downstream regions. This too is attributable to modified shear-lift modeling and shear-stress effects provided by sidewalls in the 3-D domain leading the cycle of nucleation, bubble growth, and departure to repeat more frequently. Despite this appreciable improvement, it remains difficult to capture the experimental temperature decrease in the exit region, although it is believed further improvements in capturing interfacial phenomena will resolve this discrepancy.

Fig. 13(b) shows axial variations of local heat transfer coefficient, h, with distance for the four mass velocities and heat fluxes ranging around 43% of CHF. Similar to wall temperature, predicted local heat transfer coefficient is also spatially and time-averaged over a few seconds of steady-state simulation. Predicted heat transfer coefficient is computed by dividing heat flux by temperature difference (between solid and fluid mixture temperatures, both determined through area-weighted averaging). Experimental local heat transfer coefficient is determined using a simple control volume energy balance centered on each thermocouple illustrated in Fig. 2(c). Fig. 13(b) shows 3-D computed heat transfer coefficients are well predicted over the different operating conditions. Experimental heat transfer coefficient values are seen to decrease in the entrance region, maintain a constant value in the middle region, and increase in the exit region. Heat transfer coefficient for the lowest mass velocity of $G = 176.52$ kg/m^{2}s predicted using the present 3-D simulations gradually increases with distance, as continuous thermal boundary layer development allows continu-

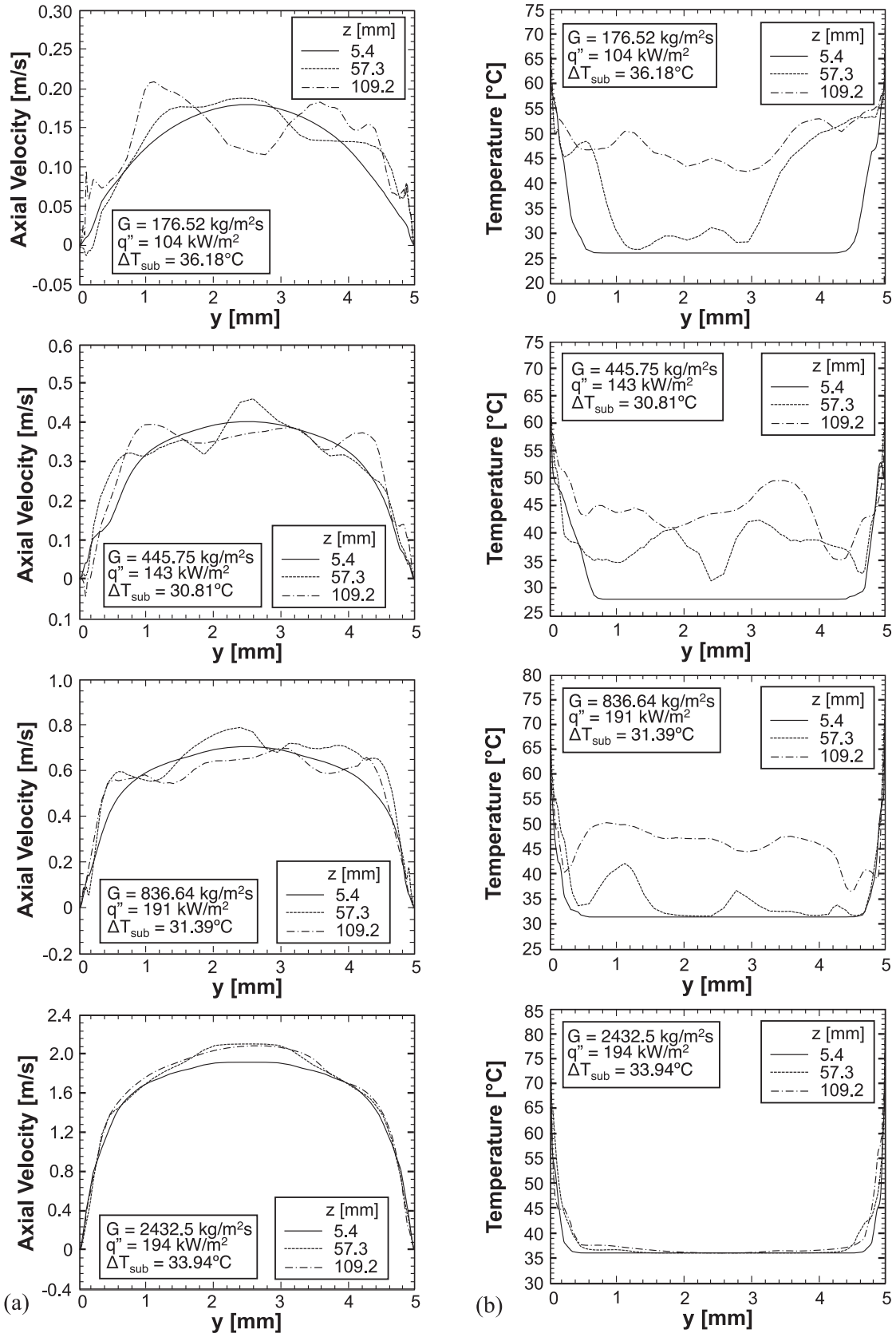

Fig. 15. Instantaneous variation of computed (a) axial velocity and (b) fluid temperature across the channel at three axial locations (entrance, middle, and exit regions) for different operating conditions.

ous phase change and bulk flow temperature increase. For higher velocities, a slight reduction in h is seen in the entrance region, followed by a slight increase along the remaining channel length (likely due to flow acceleration brought on by increasing void fraction). All 3-D predicted heat transfer coefficients are in reasonable agreement with experimental values, compared to less accurate predictions using the 2-D simulations. Due to the presence of adiabatic walls in the 3-D domain, shear stress becomes increasingly influential as mass velocity increases, resulting in increasingly better prediction of h over 2-D results. These facts further demonstrate superiority of the current 3-D approach over prior 2-D results.

Overall, deviation between measurements and 3-D predicted h is less than 400 W/m^{2}K throughout the middle region of the channel, with a minimum difference of only 0.3% for the second lowest mass velocity case. Differences between predicted and measured values are comparatively large in the upstream region, however, with maximum deviation of around 25% for the highest mass velocity case. Deviation in the entrance region is largely attributable to over-prediction of wall temperature in this portion of the channel.

Fig. 14 shows 3-D predicted average values of wall temperature and heat transfer coefficient (with averaging achieved over entire heat length) match experimental trends well, further demonstrating the effectiveness of the current 3-D computational method at predicting the boiling process more physically than prior 2-D work. In addition to inclusion of modified shear-lift force and shear stress from the sidewalls, the 3-D simulations allows for more realistic bubble shapes compared to 2-D. This leads to more physical contact area between phases as well as 3-D turbulent effects which Fig. 11 showed impacts heat transfer as well.

Despite these significant improvements, it is still difficult to model the initial boiling process of vapor growth in cavities on the heated surface as vastly differing length scales mean surface roughness effects are neglected and only bulk phenomena considered. Simulating bubble growth from physical cavities can improve prediction accuracy of wall temperature and heat transfer coefficient in the entrance region, although current computing resources are insufficient to tackle this type of multi-scale problem.

4.4. Predicted velocity and temperature profiles

Fig. 15(a) and 15(b) show, respectively, cross-sectional profiles of computed axial velocity and fluid mixture temperature at three axial locations for all four operating conditions. These profiles are instantaneously exported after steady state along a diagonal line on the cross section at each location (entrance, middle, and exit) to understand the influence of shear stress (produced by both heated and adiabatic surfaces) on local velocity and temperature.

For all cases, the velocity profiles at $z = 5.4$ mm are fairly similar to that used as inlet condition as little vapor formation has occurred. As nucleate boiling becomes appreciable in the middle region, vapor motion begins to affect profiles. Distortion from the initial profile becomes considerable as vapor bubble penetrates toward the core region of the channel following bubble departure and coalescence.

Similar to velocity profiles, fluid mixture temperature gradually develops with distance, leading to the development of a thermal boundary layer. Distortion of temperature profiles is clearly observed in the downstream region due to thermal diffusion, advection from heated surfaces, as well as vapor bubble motion. Interestingly, for temperature profiles for the case of $G = 836.64$ kg/m^{2}s, subcooled liquid replenishment is captured at $z = 109.2$ mm as there are two troughs around wall regions. As mass velocity increases, the gradients of velocity and temperature in the direction normal to the surface grows, so prediction of shear-stress transport within the boundary layer is important.

Moving along the channel across all cases appreciable increases in core temperature are observed. For the highest mass velocity, however, velocity and temperature profiles at all three locations are similar to their inlet values because bubble migration toward the center of the flow channel is suppressed by high flow inertia. Boiling still takes place in this case with small bubbles forming and lifting off from heated surfaces, but highly subcooled liquid leads to rapid condensation as they attempt to enter bulk flow. This limits their influence on velocity and temperature profiles.

5. Conclusions

The present study focused on use of a 3-D computational approach with advanced modeling for shear-lift force in ANSYS-FLUENT to predict highly subcooled nucleate flow boiling of FC-72. Four different mass velocity cases were evaluated, with heat fluxes of ~ 41–46% of CHF in each case applied to the two opposite heated surfaces of a rectangular channel in vertical upflow. Detailed information relating to the effect of shear-lift force and the ability of ANSYS-FLUENT to accurately capture its effects was provided through comparison with experimental results and analytic predictions. Comparison of 3-D with prior 2-D predictions and experimental results showed the ability of the current computational approach to surpass prior 2-D results by closely matching experimental measurements. Detailed local computational results were also utilized to highlight local phenomena (velocity and temperature profiles) not easily determined through experiments. Key findings from present study are as follows.

(1) The 3-D computational approach outlined here captures complicated subcooled flow boiling behavior along the heated portion of the channel, including vapor generation, bubble sliding, bubble departure, coalescence, and bubble break-up. Prediction of wall temperature and heat transfer coefficient is appreciably improved from prior 2-D work due to the increase of area in contact with liquid phase as well as shear-lift force and sidewall shear stress leading to more aggressive phase change.
(2) Modeling shear lift force is required to overcome innate limitations of the VOF model which employs only a single momentum equation for two phases and thus struggles to accurately represent interfacial forces. Inclusion of shear-lift force model prevents premature prediction of CHF through vapor blanketing by providing more realistic capture of bubble departure from heated walls. By enhancing physicality of bubble lift-off predictions, addition of modified shear-lift force provides more opportunity for liquid to replenish the near wall region, improving heat transfer. The 3-D nature of the present simulations also allowed for prediction of recirculation zones, further enhancing physicality of the heat transfer results.
(3) Mass transfer intensity factor r_i must be carefully tuned separately for evaporation and condensation in 3-D computational models for highly subcooled flow boiling of low conductivity fluids in macro-scale channels at high flow rates. This is due to significant interfacial heat diffusion leading to difficulty tracking interfacial behavior. Use of non-identical mass transfer intensity factors for evaporation and condensation prevents over-prediction of vapor condensation while within subcooled bulk liquid.
(4) The 3-D computational methodology outlined here exhibits capability to predict realistic flow boiling results across various operating conditions. This computational approach also shows substantial improvement over prior 2-D results. Pre-

diction of nucleate boiling in the entrance region is still a challenge, however, requiring additional modeling of boiling in small cavities to alleviate current deviations occurring in the upstream region. This is highly demanding computationally and requires further thought on how to best implement to achieve more accurate results.

Declaration of Competing Interest

None.

Acknowledgments

The authors are grateful for financial support provided by the National Aeronautics and Space Administration (NASA) under grant no. NNX17AK98G, and technical support of the NASA Glenn Research Center, Cleveland, Ohio. This work was also supported by NASA Space Technology Research Fellowship NNX15AP29H.

Supplementary materials

Supplementary material associated with this article can be found, in the online version, at doi:10.1016/j.ijheatmasstransfer.2019.119291.

References

[1] I. Mudawar, Two-phase microchannel heat sinks: theory, applications, and limitations, J. Electron. Packag. 133 (2011) 041002–041031.
[2] I. Mudawar, Recent advances in high-flux, two-phase thermal management, J. Therm. Sci. Eng. Appl. 5 (2013) 021012–021015.
[3] W. Qu, I. Mudawar, Measurement and prediction of pressure drop in two-phase micro-channel heat sinks, Int. J. Heat Mass Transf. 46 (2003) 2737–2753.
[4] S. Lee, V.S. Devahdhanush, I. Mudawar, Investigation of subcooled and saturated boiling heat transfer mechanisms, instabilities, and transient flow regime maps for large length-to-diameter ratio micro-channel heat sinks, Int. J. Heat Mass Transf. 123 (2018) 172–191.
[5] H.J. Lee, D.Y. Liu, S.-C. Yao, Flow instability of evaporative micro-channels, Int. J. Heat Mass Transf. 53 (2010) 1740–1749.
[6] T.J. LaClair, I. Mudawar, Thermal transients in a capillary evaporator prior to the initiation of boiling, Int. J. Heat Mass Transf. 43 (2000) 3937–3952.
[7] I. Mudawar, T.M. Anderson, Parametric investigation into the effects of pressure, subcooling, surface augmentation and choice of coolant on pool boiling in the design of cooling system for high-power-density electronic chips, J. Electron. Packag. 112 (1990) 375–382.
[8] I.C. Bang, S. Heung Chang, Boiling heat transfer performance and phenomena of Al2O3–water nano-fluids from a plain surface in a pool, Int. J. Heat Mass Transf. 48 (2005) 2407–2419.
[9] H.-Y. Kim, Y.G. Kim, B.H. Kang, Enhancement of natural convection and pool boiling heat transfer via ultrasonic vibration, Int. J. Heat Mass Transf. 47 (2004) 2831–2840.
[10] C.O. Gersey, I. Mudawar, Effects of heater length and orientation on the trigger mechanism for near-saturated flow boiling CHF - I. Photographic and statistical characterization of the near-wall interfacial features, Int. J. Heat Mass Transf. 38 (1995) 629–642.
[11] C.R. Kharangate, L.E. O'Neill, I. Mudawar, Effects of two-phase inlet quality, mass velocity, flow orientation, and heating perimeter on flow boiling in a rectangular channel: part 1 - Two-phase flow and heat transfer results, Int. J. Heat Mass Transf. 103 (2016) 1261–1279.
[12] C.R. Kharangate, L.E. O'Neill, I. Mudawar, Effects of two-phase inlet quality, mass velocity, flow orientation, and heating perimeter on flow boiling in a rectangular channel: part 2 - CHF experimental results and model, Int. J. Heat Mass Transf. 103 (2016) 1280–1296.
[13] S. Mukherjee, I. Mudawar, Pumpless loop for narrow channel and micro-channel boiling from vertical surfaces, J. Electron. Packag. 125 (2003) 431–441.
[14] J. Lee, I. Mudawar, Critical heat flux for subcooled flow boiling in micro-channel heat sinks, Int. J. Heat Mass Transf. 52 (2009) 3341–3352.
[15] W.P. Klinzing, J.C. Rozzi, I. Mudawar, Film and transition boiling correlations for quenching of hot surfaces with water sprays, J. Heat Treat. 9 (1992) 91–103.
[16] M. Visaria, I. Mudawar, Application of two-phase spray cooling for thermal management of electronic devices, IEEE Trans.-CPMT 32 (2009) 784–793.
[17] W.-L. Cheng, F.-Y. Han, Q.-N. Liu, R. Zhao, H.-L. Fan, Experimental and theoretical investigation of surface temperature non-uniformity of spray cooling, Energy 36 (2011) 249–257.
[18] M. Monde, T. Inoue, Critical heat flux in saturated forced convective boiling on a heated disk with multiple impinging jets, J. Heat Transf. 113 (1991) 722–727.
[19] M.E. Johns, I. Mudawar, An ultra-high power two-phase jet-impingement avionic clamshell module, J. Electron. Packag. 118 (1996) 264–270.
[20] M.K. Sung, I. Mudawar, Single-phase hybrid micro-channel/micro-jet impingement cooling, Int. J. Heat Mass Transf. 51 (2008) 4342–4352.
[21] R.W. Lockhart, R.C. Martinelli, Proposed correlation of data for isothermal two-phase, two-component flow in pipes, Chem. Eng. Prog. 45 (1949) 39–48.
[22] S.W. Churchill, R. Usagi, A general expression for the correlation of rates of transfer and other phenomena, AIChE J. 18 (1972) 1121–1128.
[23] H.J. Lee, S.Y. Lee, Pressure drop correlations for two-phase flow within horizontal rectangular channels with small heights, Int. J. Multiph. Flow 27 (2001) 783–796.
[24] S.M. Kim, I. Mudawar, Universal approach to predicting saturated flow boiling heat transfer in mini/micro-channels part I. Dryout incipience quality, Int. J. Heat Mass Transf. 64 (2013) 1226–1238.
[25] S.M. Kim, I. Mudawar, Review of databases and predictive methods for pressure drop in adiabatic, condensing and boiling mini/micro-channel flows, Int. J. Heat Mass Transf. 77 (2014) 74–97.
[26] S.M. Kim, I. Mudawar, Theoretical model for local heat transfer coefficient for annular flow boiling in circular mini/micro-channels, Int. J. Heat Mass Transf. 73 (2014) 731–742.
[27] S.M. Kim, I. Mudawar, Review of two-phase critical flow models and investigation of the relationship between choking, premature CHF, and CHF in micro-channel heat sinks, Int. J. Heat Mass Transf. 87 (2015) 497–511.
[28] C.R. Kharangate, I. Mudawar, Review of computational studies on boiling and condensation, Int. J. Heat Mass Transf. 108 (2017) 1164–1196.
[29] E.J. Davis, G.H. Anderson, The incipience of nucleate boiling in forced convection flow, AIChE J. 12 (1966) 774–780.
[30] J.-H. Wei, L.-M. Pan, D.-Q. Chen, H. Zhang, J.-J. Xu, Y.-P. Huang, Numerical simulation of bubble behaviors in subcooled flow boiling under swing motion, Nucl. Eng. Des. 241 (2011) 2898–2908.
[31] R. Zhuan, W. Wang, Flow pattern of boiling in micro-channel by numerical simulation, Int. J. Heat Mass Transf. 55 (2012) 1741–1753.
[32] M. Magnini, B. Pulvirenti, J.R. Thome, Numerical investigation of the influence of leading and sequential bubbles on slug flow boiling within a microchannel, Int. J. Therm. Sci. 71 (2013) 36–52.
[33] S. Chen, Z. Yang, Y. Duan, Y. Chen, Di Wu, Simulation of condensation flow in a rectangular microchannel, Chem. Eng. Process. 76 (2014) 60–69.
[34] J. Lee, L.E. O'Neill, S. Lee, I. Mudawar, Experimental and computational investigation on two-phase flow and heat transfer of highly subcooled flow boiling in vertical upflow, Int. J. Heat Mass Transf. 136 (2019) 1199–1216.
[35] D. Legendre, J. Magnaudet, The lift force on a spherical bubble in a viscous linear shear flow, J. Fluid Mech. 368 (1998) 81–126.
[36] G. Segre, A. Silberberg, Behaviour of macroscopic rigid spheres in Poiseuille flow Part 2. Experimental results and interpretation, J Fluid Mech. 14 (1962) 136–157.
[37] I. Mudawar, Flow boiling and flow condensation in reduced gravity, Adv. Heat Transf. 49 (2017) 225–306.
[38] H. Zhang, I. Mudawar, M.M. Hasan, Experimental and theoretical study of orientation effects on flow boiling CHF, Int. J. Heat Mass Transf. 45 (2002) 4463–4478.
[39] C. Konishi, I. Mudawar, Review of flow boiling and critical heat flux in microgravity, Int. J. Heat Mass Transf. 80 (2015) 469–493.
[40] H.K. Nahra, B.J. Motil, Measurements of shear lift force on a bubble in channel flow in microgravity, NASA/TM-2003-212113 (2013) 1–16.
[41] R. Mei, J.F. Klausner, Shear lift force on spherical bubbles, Int. J. Heat Fluid Flow 15 (1994) 62–65.
[42] W.H. Lee, A pressure iteration scheme for two-phase flow modeling, in: T.N. Veziroglu (Ed.), Multi-Phase Transport: Fundamentals, Reactor Safety, Applications, 1, Hemisphere Publishing, Washington, DC, 1980.
[43] L.E. O'Neill, I. Mudawar, M.M. Hasan, H.K. Nahra, R. Balasubramaniam, N.R. Hall, A. Lokey, J.R. Mackey, Experimental investigation into the impact of density wave oscillations on flow boiling system dynamic behavior and stability, Int. J. Heat Mass Transf. 120 (2018) 144–166.
[44] J.U. Brackbill, D.B. Kothe, C. Zemach, A continuum method for modeling surface tension, J. Comput. Phys. 100 (1992) 335–354.
[45] C.R. Kharangate, H. Lee, I. Mudawar, Computational modeling of turbulent evaporating falling films, Int. J. Heat Mass Transf. 81 (2015) 52–62.
[46] J.F. Klausner, R. Mei, D.M. Bernhard, L.Z. Zeng, Vapor bubble departure in forced convection boiling, Int. J. Heat Mass Transf. 3 (1993) 651–662.
[47] L.Z. Zeng, J.F. Klausner, D.M. Bernhard, R. Mei, A unified model for the prediction of bubble detachment diameters in boiling systems-II. Flow boiling, Int. J. Heat Mass Transf. 36 (1993) 2271–2279.
[48] S.S. Rabha, V.V. Buwa, Volume-of-fluid (VOF) simulations of rise of single/multiple bubbles in sheared liquids, Chem. Eng. Sci. 65 (2010) 527–537.
[49] P.G. Saffman, The lift on a small sphere in a slow shear flow, J. Fluid Mech. 22 (1965) 385–400.
[50] T.R. Auton, The lift force on a spherical body in a rotational flow, J. Fluid Mech. 183 (1987) 199–218.
[51] R.W. Schrage, A Theoretical Study of Interphase Mass Transfer, Columbia University Press, New York, 1953.
[52] S. Chen, Z. Yang, Y. Duan, Y. Chen, D. Wu, Simulation of condensation flow in a rectangular microchannel, Chem. Eng. Process. 76 (2014) 60–69.
[53] H.L. Wu, X.F. Peng, P. Ye, Y. Eric Gong, Simulation of refrigerant flow boiling in serpentine tube, Int. J. Heat Mass Transf. 50 (2007) 1186–1195.
[54] Z. Yang, X.F. Peng, P. Ye, Numerical and experimental investigation of two phase flow during boiling in a coiled tube, Int. J. Heat Mass Transf. 51 (2008) 1003–1016.

[55] M. Bahreini, A. Ramiar, A.A. Ranjbar, Numerical simulation of subcooled flow boiling under conjugate heat transfer and microgravity condition in a vertical mini channel, Appl. Therm. Eng. 113 (2017) 170–185.
[56] D. Lorenzini, Y.K. Joshi, Computational fluid dynamics modeling of flow boiling in microchannels with nonuniform heat flux, J. Heat Transf. 140 (2018) 011501–1.
[57] S.C.K. De Schepper, G.J. Heynderickx, G.B. Marin, Modeling the evaporation of a hydrocarbon feedstock in the convection section of a steam cracker, Comput. Chem. Eng. 33 (2009) 122–132.
[58] C. Fang, M. David, A. Rogacs, K. Goodson, Volume of fluid simulation of boiling two-phase flow in a vapor-venting microchannel, Front. Heat Mass Transf. 1 (2010) 0132002.
[59] A. Alizadehdakhel, M. Rahimi, A.A. Alsairafi, CFD modeling of flow and heat transfer in a thermosyphon, Int. Commun. Heat Mass Transf. 37 (2010) 312–318.
[60] ANSYS FLUENT Theory Guide, ANSYS Inc., Canonburg, PA, 2009.